Deciphering Multi-way Interactions in the Human Genome

Gabrielle A. Dotson[1,†], Stephen Lindsly[1,†], Anthony Cicalo[1,†], Can Chen[2,3,4,†], Sam Dilworth[5], Charles Ryan[7,8], Sivakumar Jeyarajan[1], Walter Meixner[1], Nicholas Beckloff[6], Amit Surana[9], Max Wicha[10], Lindsey A. Muir[1], and Indika Rajapakse[1,2,*]

[1]Department of Computational Medicine and Bioinformatics, University of Michigan, Ann Arbor, MI 48109 USA
[2]Department of Mathematics, University of Michigan, Ann Arbor, MI 48109 USA
[3]Department of Electrical Engineering and Computer Science, University of Michigan, Ann Arbor 48109 USA
[4]Channing Division of Network Medicine, Brigham and Women's Hospital and Harvard Medical School, Boston, MA 02115 USA
[5]iReprogram, Ann Arbor, MI 48105 USA
[6]Oxford Nanopore Technologies, Oxford, OX4 4DQ UK
[7]Medical Scientist Training Program, University of Michigan, Ann Arbor, MI 48109 USA
[8]Program in Cellular and Molecular Biology, University of Michigan, Ann Arbor, MI 48109 USA
[9]Raytheon Technologies Research Center, East Hartford, CT 06108 USA
[10]Department of Hematology/Oncology, University of Michigan, Ann Arbor, MI 48109 USA
[†]These authors contributed equally to this work.
[*]To whom correspondence should be addressed (indikar@umich.edu).

Abstract

Chromatin architecture, a key regulator of gene expression, can be inferred using chromatin contact data from chromosome conformation capture, or Hi-C. However, classical Hi-C does not preserve multi-way contacts. Here we use long sequencing reads to map genome-wide multi-way contacts and investigate higher order chromatin organization in the human genome. We use hypergraph theory for data representation and analysis, and quantify higher order structures in neonatal fibroblasts, biopsied adult fibroblasts, and B lymphocytes. By integrating multi-way contacts with chromatin accessibility, gene expression, and transcription factor binding, we introduce a data-driven method to identify cell type-specific transcription clusters. We provide transcription factor-mediated functional building blocks for cell identity that serve as a global signature for cell types.

1 Introduction

Structural features of the genome are integral to the regulation of gene expression and corresponding generation of cellular phenotypes [1, 2, 3]. Aspects of genome structure have been inferred by studying genomic regions that are in close physical proximity. Chromosome conformation capture (3C)-based methods capture these interactions (contacts) through chemical fixation, digestion of DNA, and proximity ligation, followed by sequencing of ligated DNA to identify genomic regions that are in contact. A variety of cell types have now been characterized using Hi-C, a genome-wide 3C-based method, adding substantially to our understanding of genome architecture. However, limitations on read length during sequencing lead to over-representation of simple interactions, predominantly pairwise. Identification of more complex, higher-order interactions can help us build a more complete set of principles of genome architecture.

Multi-way contacts have been identified using targeted 3C-based methods [4, 5, 6], through inference from pairwise contacts [7], and on occasion using classical Hi-C [8]. Ligation-free approaches, such as GAM and SPRITE, have recently enabled large scale capture of multi-way interactions [9, 10, 11], though comparisons of different methods find under- and over-representation of higher order contacts in the absence of proximity ligation [12, 13]. A recent extension of Hi-C preserves multi-way interactions and uses sequencing of long reads (e.g. Pore-C) [12] to unambiguously identify sets of contacts among multiple loci. Multi-contact 4C sequencing (MC-4C) also uses long-read sequencing to capture contact complexity [14], however, it was designed to capture local topology for individual genes and regulatory regions and does not generate multi-way contacts genomewide. While direct capture of multi-way contacts can clarify higher order structures in the genome, new frameworks are needed to address unique analysis and representation challenges posed by the multi-way data.

To address this gap, we generated Pore-C data from neonatal and biopsied adult fibroblasts and collected publicly available Pore-C data for B lymphocytes [12] and constructed hypergraphs to represent the multidimensional relationships of multi-way contacts among loci. Hypergraphs are similar to graphs, but hypergraphs contain hyperedges instead of edges. Hyperedges can connect any number of nodes at once, while edges can only connect two nodes [15, 16, 17]. Prior work on neural networks highlights the utility of hypergraph representation learning to denoise and analyze existing multi-way contact data and to predict *de novo* multi-way contacts [18]. Here, we use incidence matrix-based representation and analysis of multi-way chromatin structure directly captured by Pore-C data, which is mathematically simple and computationally efficient, and yet can provide new insights into genome architecture.

In our hypergraph framework, nodes are genomic loci and hyperedges are multi-way contacts among loci. In our incidence matrices, rows are genomic loci and columns are individual hyperedges. This representation enabled quantitative measurements of chromatin architecture through hypergraph entropy and the comparison of different cell types through hypergraph similarity measures. In addition, we integrated Pore-C with other data modalities to discover biologically relevant multi-way interactions, which we term transcription clusters. The cell-type specific transcription clusters we identified support a role in maintaining cell identity, consistent with prior work on transcriptional hubs or factories [19, 20, 21, 22, 23]. Furthermore, the formation of transcription clusters in the nucleus is consistent with small world phenomena in networked systems [24, 25].

We use the following definitions. **Entropy**: a measure of structural order in the genome. **Hyperedge**: an extension of edges where each hyperedge can contain any number of nodes (multi-way contact). **Hypergraph**: an extension of graphs containing multiple hyperedges. **Hypergraph motifs**: an extension of network motifs that describe connectivity patterns of 3-way, 4-way, ..., n-way hyperedges. **Incidence matrix**: a representation for hypergraphs where rows are nodes and columns are hyperedges. **Transcription cluster**: a group of genomic loci that colocalize for efficient gene transcription.

2 Results

2.1 Capturing Multi-way Contacts

We conducted Pore-C experiments using adult human dermal fibroblasts obtained from a skin biopsy and neonatal human dermal fibroblasts, and obtained additional publicly available Pore-C data from B lymphocytes [12]. The experimental protocol for Pore-C is similar to Hi-C, including cross-linking, restriction digestion, and ligation of adjacent ends followed by sequencing (Figure 1A). Alignment of Pore-C long reads to the genome enables fragment identification and classification of multi-way contacts (Figure 1B).

Hypergraphs represent multi-way contacts, where individual hyperedges contain at least two loci (Figure 1C, left). Hypergraphs provide a simple and concise way to depict multi-way contacts and allow for abstract representations of genome structure. Computationally, we represent multi-way contacts as incidence matrices (Figure 1C, right). For Hi-C data, adjacency matrices are useful for assembly of pairwise genomic contacts. However, since rows and columns represent individual loci, adjacency matrices cannot be used for multi-way contacts in Pore-C data. In contrast, incidence matrices permit more than two loci per contact and provide a clear visualization of multi-way contacts. Multi-way contacts can also be decomposed into pairwise contacts, similar to those in Hi-C, by extracting all pairwise combinations of loci (Figure 1D).

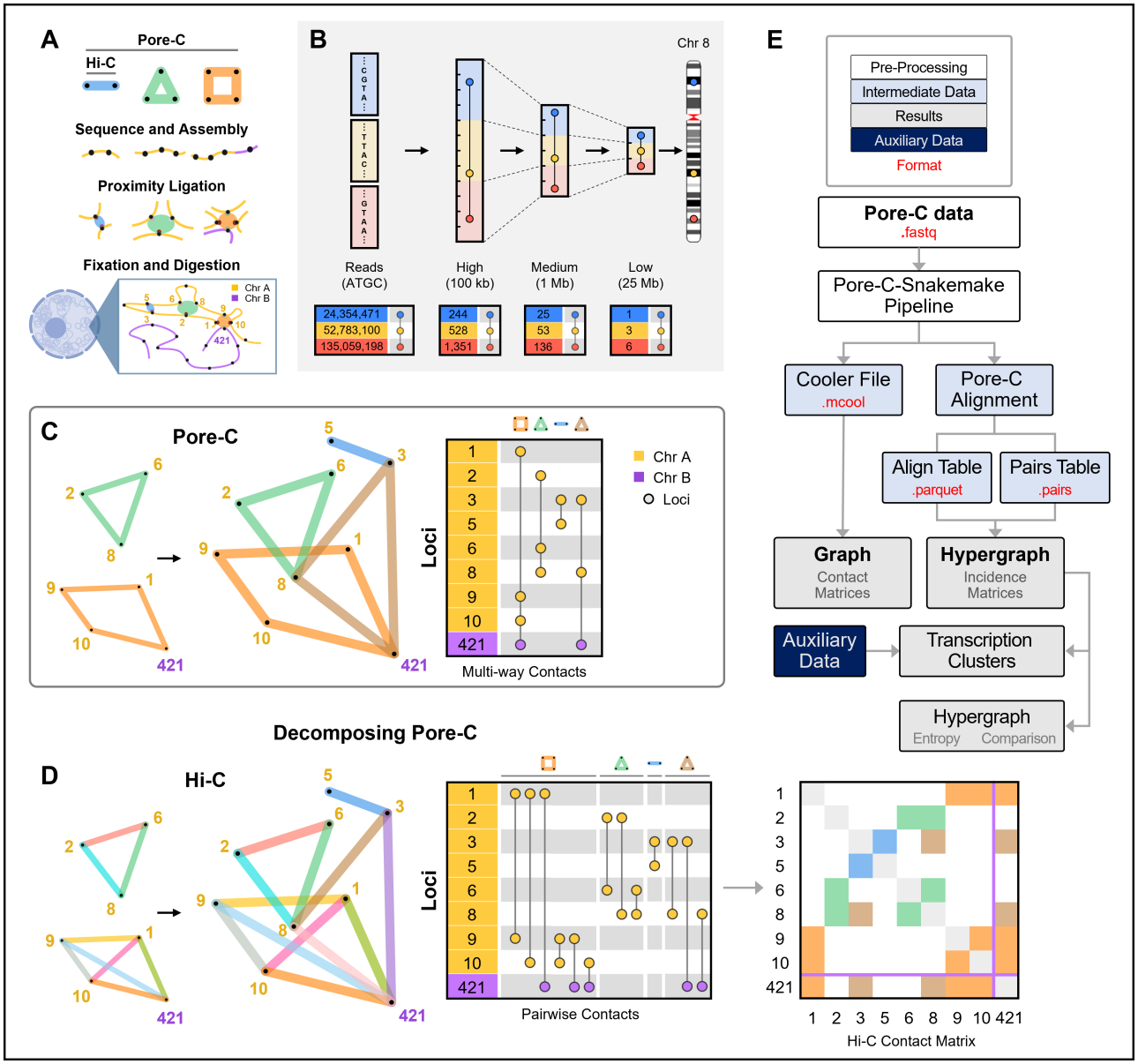

Figure 1: Pore-C experimental and data workflow. (A) The Pore-C experimental protocol, which captures pairwise and multi-way contacts (*Materials and Methods*). (B) Representation of multi-way contacts at different resolutions (top). Incidence matrix visualizations of a representative example from Chromosome 8 in adult human fibroblasts at each resolution (bottom). The numbers in the left columns represent the location of each genomic locus present in a multi-way contact, where values are either the chromosome base-pair position (read-level) or the bin into which the locus was placed (binning at 100 kb, 1 Mb, or 25 Mb). (C) Hypergraph representation of Pore-C contacts (left) and an incidence matrix (right) of four multi-way contacts within (yellow-to-yellow) and between (yellow-to-purple) chromosomes. Contacts correspond to examples from A. The numbers in the left column represent genomic bins in which a locus resides. Each vertical line represents a multi-way contact, with nodes at participating genomic loci. (D) Multi-way contacts can be decomposed into pairwise contacts. Decomposed multi-way contacts can be represented using graphs (left) or incidence matrices (middle), which when decomposed are interchangeable with traditional Hi-C contact matrices (right). Contacts correspond to examples from A and C. (E) Flowchart overview of the computational framework. Descriptions of file type formats (red text) are in Table S1.

2.2 Decomposing Multi-way Contacts

From our Pore-C experiments using adult human dermal fibroblasts, neonatal human dermal fibroblasts, and additional publicly available Pore-C data from B lymphocytes, we constructed hypergraphs at multiple resolutions (read level, 100 kb, 1 Mb, and 25 Mb) [12]. We first analyzed individual chromosomes at 100 kb resolution by decomposing multi-way contacts into their pairwise contacts. Decomposing Pore-C data into pairwise contacts provides more information than Hi-C, as each Pore-C read can contain many pairwise contacts [12]. It also allows us to identify topologically associated domains (TADs) using established methods (*Materials and Methods*) [26, 27, 28]. We demonstrate identification of TAD boundaries from

decomposed multi-way contacts and show intra- and inter-TAD relationships using multi-way contacts (Figures 2, S1). The loci that frequently participate in these multi-way contacts give rise to the block-like pattern of chromatin interactions often seen in Hi-C data.

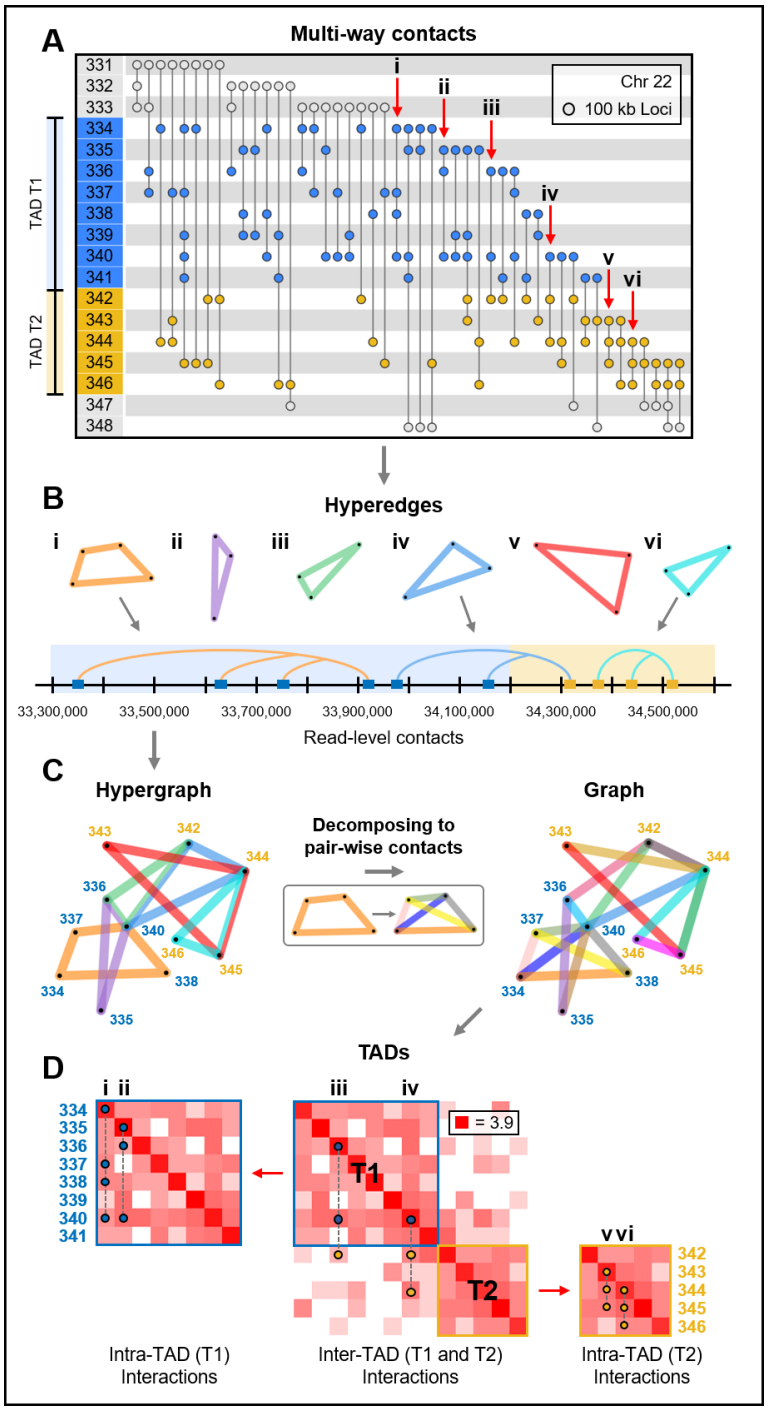

Figure 2: Local organization of the genome. (A) Incidence matrix visualization of a region in Chromosome 22 from adult fibroblasts (V1-V4). The numbers in the left column represent genomic loci at 100 kb resolution, vertical lines represent multi-way contacts, where nodes indicate the corresponding locus' participation in this contact. The blue and yellow regions represent two TADs, T1 and T2. The six contacts, denoted by the labels i-vi, are used as examples to show intra- and inter-TAD contacts in B, C, and D. (B) Hyperedge and read-level visualizations of the multi-way contacts i-vi from the incidence matrix in A. Blue and yellow shaded areas (bottom) indicate which TAD each locus corresponds to. (C) A hypergraph is constructed using the hyperedges from B (multi-way contacts i-vi from A). The hypergraph is decomposed into its pairwise contacts in order to be represented as a graph. (D) Contact frequency matrices were constructed by separating all multi-way contacts within this region of Chromosome 22 into their pairwise combinations. TADs were computed from the pairwise contacts using the methods from [28]. Example multi-way contacts i-vi are superimposed onto the contact frequency matrices. Multi-way contacts in this figure were determined at 100 kb resolution after noise reduction, originally derived from read-level multi-way contacts (*Materials and Methods*).

2.3 Chromosomes as Hypergraphs

To gain a better understanding of genome structure with multi-way contacts, we constructed hypergraphs for entire chromosomes at 1 Mb resolution. We show an incidence matrix of Chromosome 22 as an example in Figure 3A, and in Figure 3B, we visualize the distribution of 1 Mb contacts at multiple orders (2-way contacts, 3-way contacts, etc.) on Chromosomes 22. Figure 3C highlights the most common intra-chromosomal multi-way contacts on Chromosome 22 using multi-way contact "motifs", which we use as a simplified way to show hyperedges. Figure 3D shows how multi-way contacts at lower resolutions (25 Mb, 1 Mb) are composed of many multi-way contacts at higher resolutions (100 kb, read level), and Figure 3E visualizes the multi-way contacts contained in Figure 3D as a hypergraph.

We also identified multi-way contacts that contain loci from multiple chromosomes. These inter-chromosomal multi-way contacts can be seen at 1 Mb resolution in Figure 3F and in 25 Mb resolution for both adult fibroblasts and B lymphocytes in Figure 4A and 4B, respectively. Figure 4 gives a summary of the entire genome's multi-way contacts, by showing the most common intra- and inter-chromosomal multi-way contacts across all chromosomes. We highlight examples of multi-way contacts with loci that are contained within a single chromosome ("intra only"), spread across unique chromosomes ("inter only"), and a mix of both within and between chromosomes ("intra and inter"). We note that many of the "inter only" contacts observed in Figure 4 may also have intra-chromosomal contacts when viewed at a higher resolution, similar to Figure 3D. Finally, we found the most common inter-chromosomal multi-way contacts across all chromosomes, which we summarize with five example chromosomes in Figure 5 using multi-way contact motifs. These multi-way contacts between distant genomic loci may offer insights into the higher-order structural patterning of the genome and its relationship with transcriptional regulation.

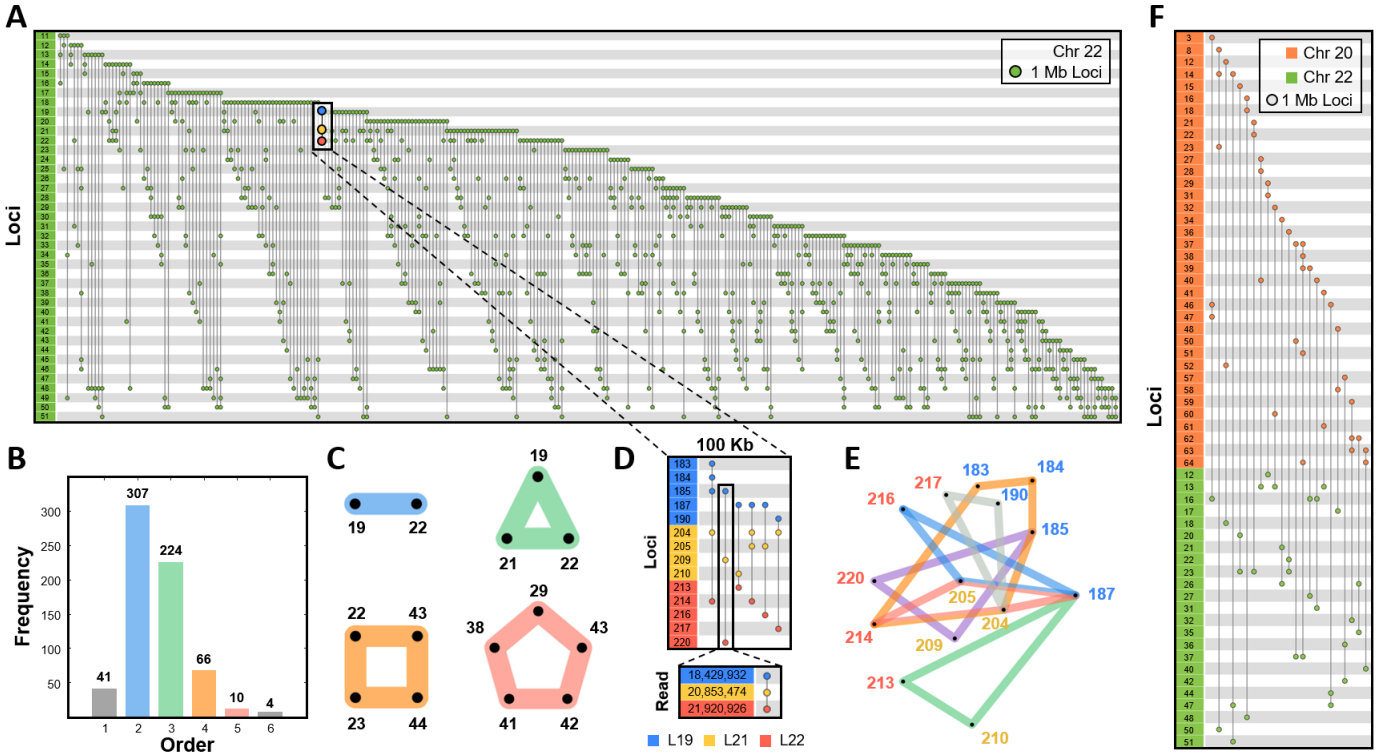

Figure 3: Patterning of intra- and inter-chromosomal contacts. (A) Incidence matrix visualization of Chromosome 22 in adult fibroblasts. The numbers in the left column represent genomic loci at 1 Mb resolution. Each vertical line represents a multi-way contact, in which the nodes indicate the corresponding locus' participation in this contact. (B) Frequencies of Pore-C contacts in Chromosome 22. Bars are colored according to the order of contact. Blue, green, orange, and red correspond to 2-way, 3-way, 4-way, and 5-way contacts. (C) The most common 2-way, 3-way, 4-way, and 5-way intra-chromosome contacts within Chromosome 22 are represented as motifs, color-coded similarly to B. (D) Zoomed in incidence matrix visualization in 100 kb resolution shows the multi-way contacts between three 1 Mb loci: L19 (blue), L21 (yellow), and L22 (red). An example 100 kb resolution multi-way contact is zoomed to read-level resolution. (E) Hypergraph representation of the 100 kb multi-way contacts from D. Blue, yellow, and red labels correspond to loci L19, L21, and L22, respectively. (F) Incidence matrix visualization of the inter-chromosomal multi-way contacts between Chromosome 20 (orange) and Chromosome 22 (green) in 1 Mb resolution. Within this figure, all data are from one adult fibroblast sequencing run (V2) and multi-way contacts were determined after noise reduction at 1 Mb or 100 kb resolution accordingly (*Materials and Methods*).

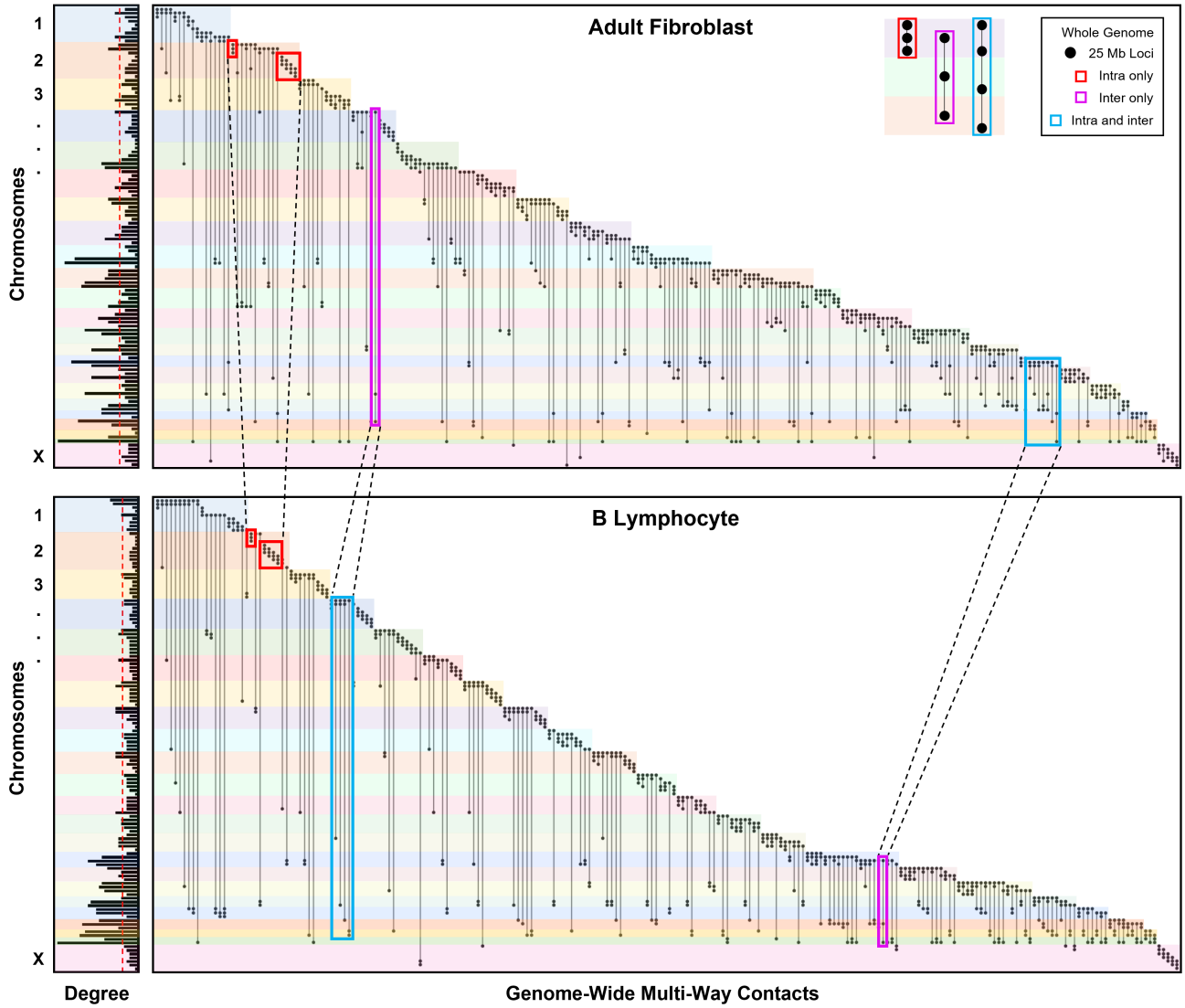

Figure 4: Genome-wide patterning of multi-way contacts. Incidence matrix visualization of the top 10 most common multi-way contacts per chromosome. Matrices are constructed at 25 Mb resolution for both adult fibroblasts (top, V1-V4) and B lymphocytes (bottom). Specifically, 5 intra-chromosomal and 5 inter-chromosomal multi-way contacts were identified for each chromosome with no repeated contacts. If 5 unique intra-chromosomal multi-way contacts are not possible in a chromosome, they are supplemented with additional inter-chromosomal contacts. Vertical lines represent multi-way contacts, nodes indicate the corresponding locus' participation in a multi-way contact, and color-coded rows delineate chromosomes. Highlighted boxes indicate example intra-chromosomal contacts (red), inter-chromosomal contacts (magenta), and combinations of intra- and inter-chromosomal contacts (blue). Examples for each type of contact are shown in the top right corner. Multi-way contacts of specific regions are compared between cell types by connecting highlighted boxes with black dashed lines, emphasizing similarities and differences between adult fibroblasts and B lymphocytes. Normalized degree of loci participating in the top 10 most common multi-way contacts for each chromosome in adult fibroblast and B lymphocytes are shown on the left. Red dashed lines indicate the mean degree for adult fibroblasts and B lymphocytes (top and bottom, respectively). Genomic loci that do not participate in the top 10 most common multi-way contacts for adult fibroblasts or B lymphocytes were removed from their respective incidence matrices and degree plots. Multi-way contacts were determined at 25 Mb resolution after noise reduction (*Materials and Methods*).

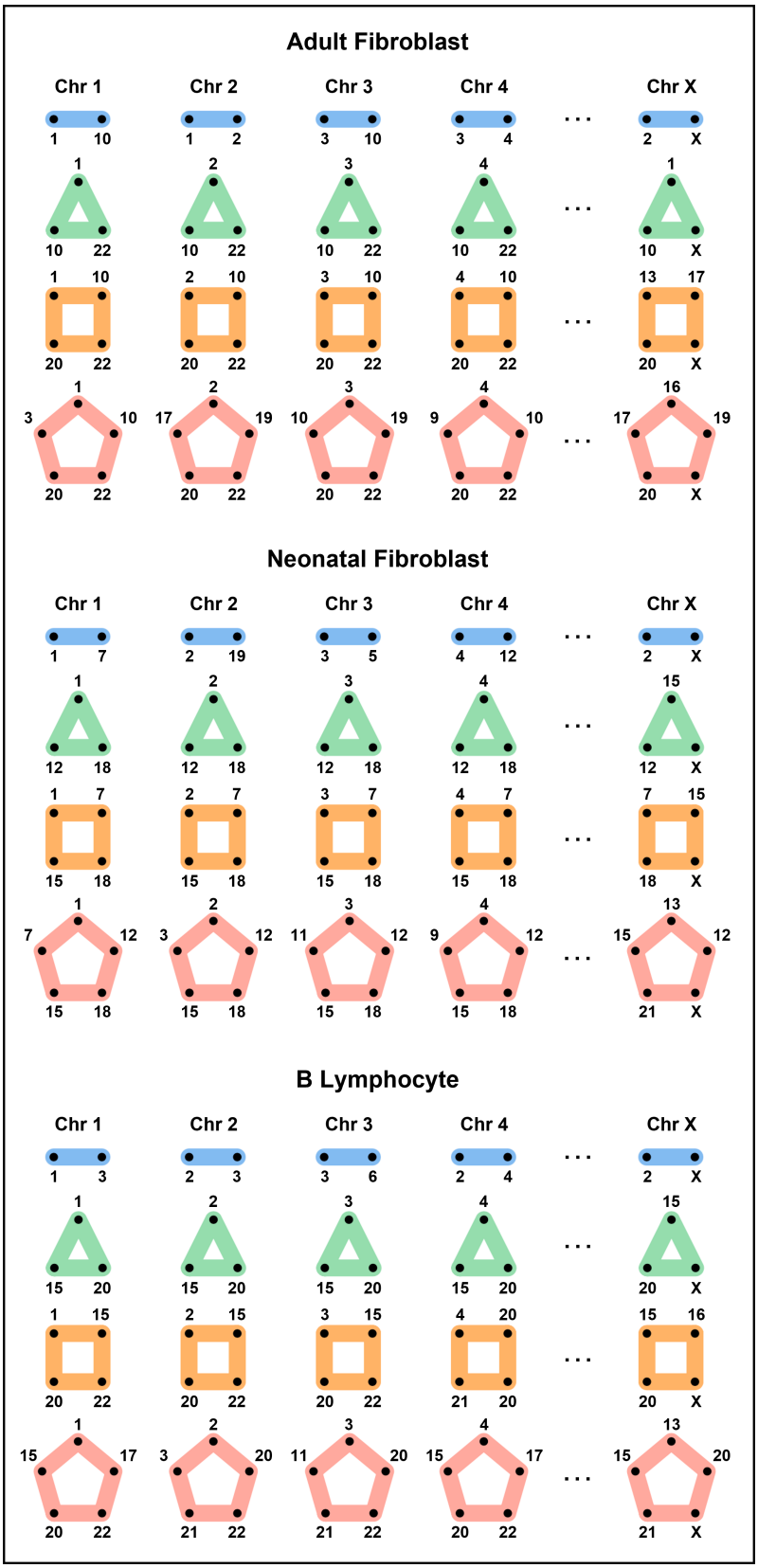

Figure 5: Inter-chromosomal interactions. The most common 2-way, 3-way, 4-way, and 5-way inter-chromosome combinations for each chromosome are represented using motifs from adult fibroblasts (top), neonatal fibroblasts (center), and B lymphocytes (bottom). Rows represent the combinations of 2-way, 3-way, 4-way, and 5-way inter-chromosomal interactions, and columns are the chromosomes. Inter-chromosomal combinations are determined using 25 Mb resolution multi-way contacts after noise reduction (*Materials and Methods*) and are normalized by chromosome length. Here we only consider unique chromosome instances (i.e. multiple loci in a single chromosome are ignored).

2.4 Transcription Clusters

We use the following definitions: **Transcription cluster**: a group of genomic loci that colocalize for efficient gene transcription. **Master regulator**: a self-regulating transcription factor that binds its gene analog. **Specialized transcription cluster**: a transcription cluster where at least one master regulator binds. **Self-sustaining transcription cluster:** a transcription cluster where a TF binds and its gene analog is expressed.

Genes are transcribed in short sporadic bursts in areas with high concentrations of transcriptional machinery [29, 30, 31], including transcriptionally engaged polymerase and accumulated transcription factors (TFs). Colocalization of multiple genomic loci in these areas may facilitate more efficient transcription, which is supported by studies using fluorescence in situ hybridization (FISH) that show colocalization during active transcription [19]. Simulations also provide evidence that genomic loci that are bound by common transcription factors can self-assemble into clusters, forming structural patterns commonly observed in Hi-C data [31]. We refer to these instances of highly concentrated areas of transcriptional machinery and genomic loci as *transcription clusters*. The colocalization of multiple genomic loci naturally leads to multi-way contacts, but these interactions cannot be fully captured from the pairwise contacts of Hi-C. Multi-way contacts derived from Pore-C reads can detect interactions between many genomic loci, and are well suited for identifying potential transcription clusters (Figure 6).

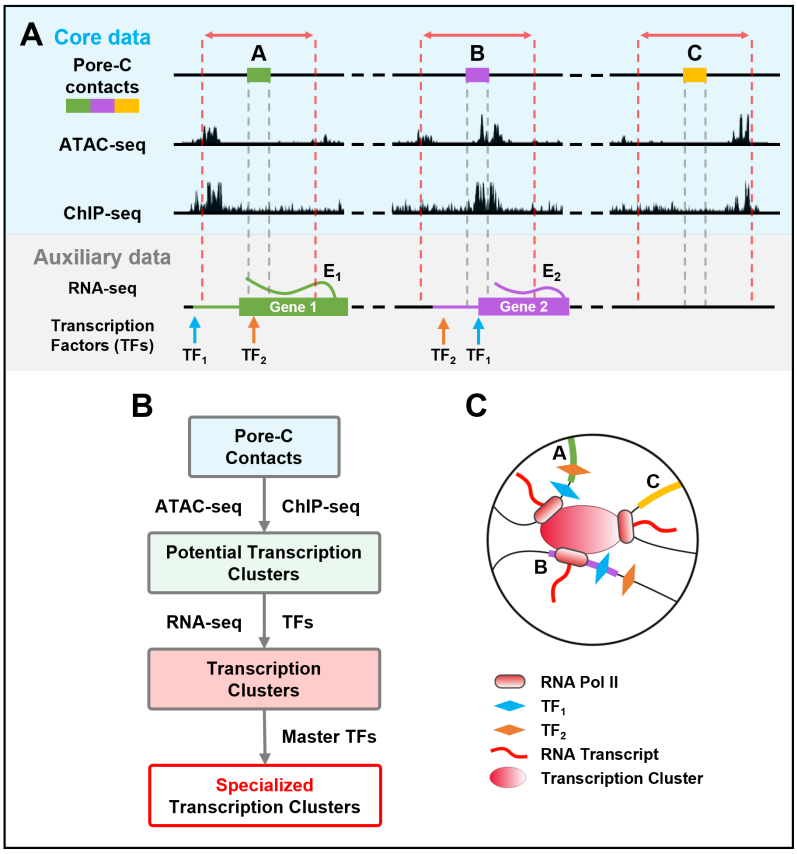

Figure 6: Data-driven identification of transcription clusters. (A) Blue shaded area: A 5 kb region before and after each locus in a Pore-C read (region between red dashed lines) is queried for chromatin accessibility and RNA Pol II binding (ATAC-seq and ChIP-seq, respectively). Multi-way contacts between accessible loci that have ≥ 1 instance of RNA Pol II binding are indicative of potential transcription clusters. Gray shaded area: Gene expression (RNA-seq, E_1 for gene 1 and E_2 for gene 2, respectively) and transcription factor binding sites (TF_1 and TF_2) are integrated to determine potential coexpression and coregulation within multi-way contacts with multiple genes. Transcription factor binding sites are queried $\pm$ 5 kb from the gene's transcription start site (*Materials and Methods*). Genes are colored based on the overlapping Pore-C locus, and the extended horizontal line from each gene represents the 5 kb flanking region used to query transcription factor binding sites. (B) Pipeline for extracting transcription clusters (*Supplementary Materials*). (C) Schematic representation of a transcription cluster.

As actively transcribed regions are accessible and transcription is carried out by locally-bound RNA Pol II [32], we require all loci in a candidate transcription cluster to be accessible, evidenced by ATAC-seq, and at least one of those loci to contain an RNA Pol II ChIP-seq signature. Using these criteria, we identified 12,364, 16,080, and 16,527 potential transcription clusters from neonatal fibroblasts, adult fibroblasts, and B lymphocytes, respectively (Table 1, *Materials and Methods*). The majority

of these clusters involved at least one expressed gene (94.2% in neonatal fibroblasts, 95.0% in adult fibroblasts, 90.5% in B lymphocytes) as well as at least two expressed genes (69.6% in neonatal fibroblasts, 71.9% in adult fibroblasts, 58.7% in B lymphocytes). While investigating the colocalization of expressed genes in transcription clusters, we found that over half of clusters containing multiple expressed genes had common transcription factors based on binding motifs in fibroblasts (61.9% in neonatal fibroblasts, 65.2% in adult fibroblasts) and that over half of these common transcription factors were master regulators (55.9% in neonatal fibroblasts, 63.4% in adult fibroblasts). These proportions were slightly lower in B lymphocytes where we observed that 50.0% of clusters containing multiple expressed genes had common transcription factors while 46.8% of these common transcription factors were master regulators. Example transcription clusters derived from 3-way, 4-way, and 5-way contacts in fibroblasts and B lymphocytes are shown in Figure 7. Transcription clusters contained at least two expressed genes with at least one common transcription factor binding motif.

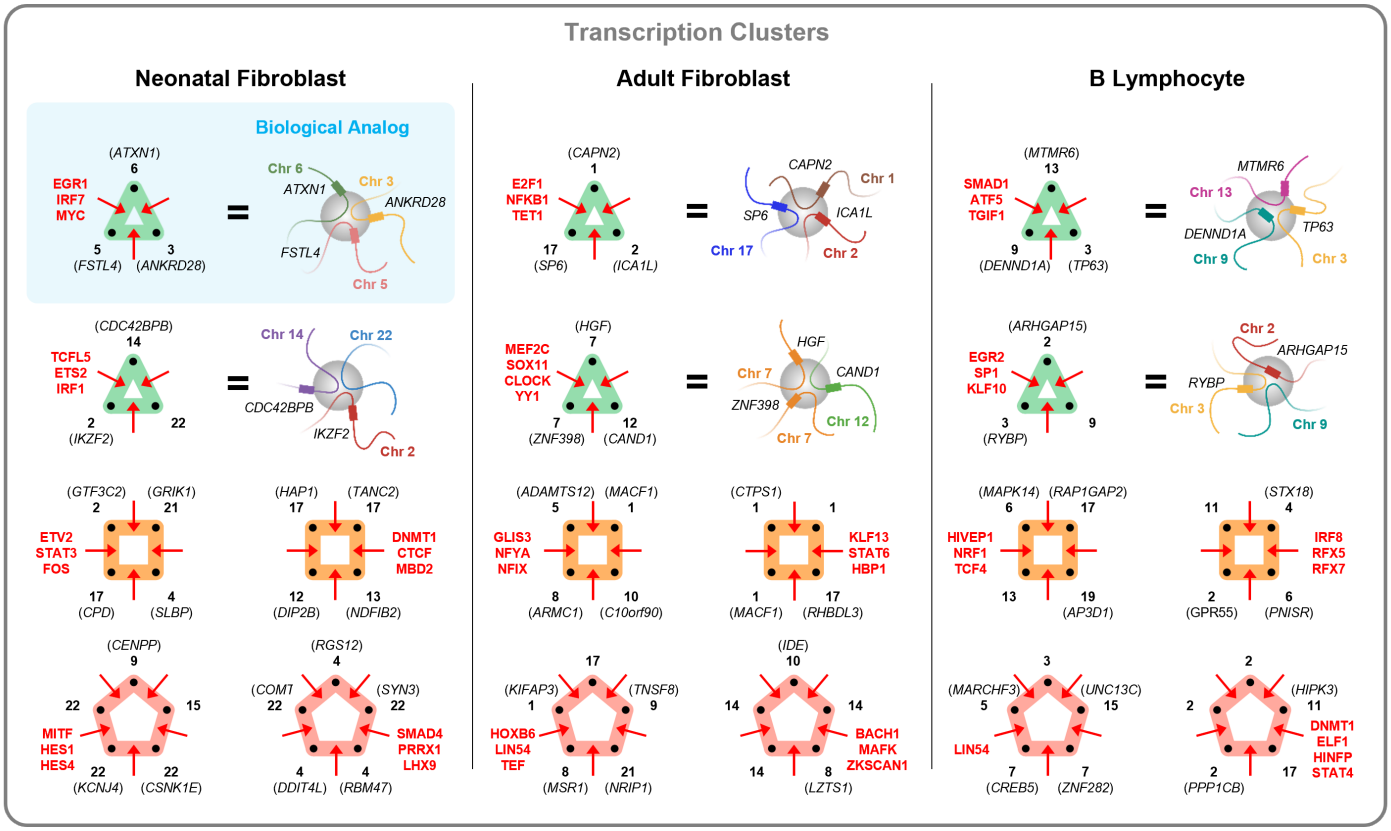

Figure 7: Example transcription clusters. Six examples of transcription clusters are shown for neonatal fibroblasts (left), adult fibroblasts (center), and B lymphocytes (right) as multi-way contacts (hypergraph motifs). Black labels indicate genes and chromosomes (bold). Red labels correspond to transcription factors shared between the majority of genes within the transcription cluster. For three-way contacts (green motifs), we highlight the transcription clusters' biological analog (blue-shaded box), showing how fragments of chromatin fold and congregate at a common transcription cluster (grey sphere). Each node (black dot) of the hyperedge and its denoted chromosome and gene in the hypergraph motif corresponds to a single chromatin fragment, colored according to chromosome, in the biological analog. Thus, a three-way hyperedge is depicted by three chromatin fragments in close spatial proximity. Multi-way contacts used for adult and neonatal fibroblasts include all experiments (V1-V4). Examples were selected from the subset of multi-way contacts summarized in the "Clusters with Common TFs" column of Table 1.

We tested the criteria for potential transcription clusters for statistical significance (*Materials and Methods*). That is, we tested whether the identified transcription clusters are more likely to include genes, and if these genes were more likely to share common transcription factors, than random multi-way contacts. We found that the identified transcription clusters were significantly more likely to include ≥ 1 gene and ≥ 2 genes than random multi-way contacts ($p < 0.01$). In addition, transcription clusters containing ≥ 2 genes were significantly more likely to have transcription factors and master regulators in common ($p < 0.01$). After testing all orders of multi-way transcription clusters together, we also tested the 3-way, 4-way, 5-way, and 6-way (or more) cases individually. We found that all cases were statistically significant ($p < 0.01$) except for clusters with common transcription factors or master regulators in the 6-way (or more) case for both fibroblasts and B lymphocytes. We hypothesize that these cases were not statistically significant due to the large number of loci, naturally leading to an increased overlap with genes. This increases the likelihood that at least two genes will have common transcription factors or master regulators. Over half of the transcription clusters where the majority of genes contained common transcription factors

also contained at least one enhancer in adult fibroblasts (98.2%) and B lymphocytes (87.9%), further suggesting regulatory function within these multi-way contacts [33, 34] (Table S2). In contrast, only 11.6% of transcription clusters in neonatal fibroblasts exhibited the same properties, which may be a factor of the significantly sparser enhancer annotation available for this cell type compared to the others from the EnhancerAtlas 2.0 database.

To understand how our transcription clusters aligned with factors that have known involvement in chromatin architecture and transcriptional regulation, we evaluated CCCTC-binding factor (CTCF) for binding using ChIP-seq data. CTCF specifically mediates chromatin looping and TAD boundary insulation [35, 36] and binds generously throughout the genome [27]. We found significantly higher CTCF binding in our identified transcription clusters compared to multi-way contacts that were not classified as transcription clusters (Figure S3). In adult and neonatal fibroblasts, CTCF binding was nearly two-fold greater in transcription clusters compared to randomly selected multi-way contacts (80% vs. 45% and 81% vs. 47%). In B lymphocytes, CTCF binding was present at 82% of transcription clusters compared to 59% of random multi-way contacts. We additionally investigated cohesin for its colocalization with CTCF and involvement in regulation of chromatin architecture, such as chromatin loop extrusion [37, 38, 39, 40]. In particular, the cohesin subunits RAD21 and SMC3 have been previously linked to CTCF-mediated transcriptional regulation [27]. ChIP-seq data showed preferential binding of RAD21 and SMC3 at transcription clusters compared to random multi-way contacts in adult fibroblasts (79% vs. 42% for RAD21, 71% vs. 37% for SMC3, $p < 0.01$) and B lymphocytes (76% vs. 55% for RAD21, 79% vs. 53% for SMC3, $p < 0.01$) (Figure S3). Together these data suggest that the identified transcription clusters are important sites of transcriptional regulation, and support a model in which CTCF and cohesin actively mediate multi-way interactions.

We next sought to determine which TFs might be involved in cell type-specific regulation in transcription clusters. For each cell type, we ranked expressed TFs by frequency of binding sites across transcription clusters. Among TFs with the most frequent binding sites, 39% were shared across all three cell types, compared to 72% between adult and neonatal fibroblasts (Table S6). Fibroblast and B lymphocyte TF binding sites had less overlap, at 52% (adult) and 45% (neonatal), than binding sites between fibroblasts, supporting cell type-specific regulation of transcription cluster subsets. Of 18 TFs whose binding sites were unique to the transcription clusters of neonatal fibroblasts, the most frequently occurring was RARB, found at 10.2% of clusters, while in adult fibroblasts, binding sites for ZNF667 were the most frequent among 14 TFs at 6.7% of transcription clusters. In B lymphocytes, binding sites for TFEC were the most frequent among 161 TFs at 7.6% of transcription clusters. Prior studies support the cell type-specific roles of these uniquely-binding TFs in fibroblasts and B lymphocytes [41, 42].

Given the role of TFs in coordinating transcription among clusters of genes [21, 43], we hypothesized that TF loci might feature in a subset of transcription clusters. To investigate this question, we looked for the binding motif and locus for a given TF within the same transcription cluster, defining this class as a self-sustaining transcription cluster (Figure 8A-B). We identified nine, eight, and thirteen self-sustaining transcription clusters in adult fibroblasts, neonatal fibroblasts, and B lymphocytes, respectively (Table S7). In adult fibroblasts, we observed that the binding motif for FOXO3, a master regulator, exists at a 4-way transcription cluster expressing the *FOXO3* gene. The neonatal fibroblast and B lymphocyte datasets had a self-sustaining transcription cluster in common where STAT3 had a binding motif and the *STAT3* gene was expressed. While self-sustaining transcription clusters demonstrate the capacity for a TF to regulate itself, not every TF co-occupying a transcription cluster with its gene analog is classified as a master regulator (Table S7). Therefore, we further stratify these clusters into self-sustaining transcription clusters where the TF is a master regulator and thus binds its gene analog (stronger coupling) and self-sustaining transcription clusters where the TF binds in the cluster but not at is gene analog (weaker coupling). We propose that these strongly-coupled self-sustaining transcription clusters are 'core' transcription clusters that serve as transcriptional signatures for a cell type. It also follows that strongly-coupled self-sustaining transcription clusters are specialized transcription clusters (Figure S4). We then considered two classes of analog-independent transcription clusters - where either a TF and its gene analog occupy different clusters (Figure 8C) or a TF occupies a cluster, but its gene analog occupies no cluster (Figure 8D). Since both the TF and gene analog belong to transcription clusters in Figure 8C, they are coupled, though lesser so than either class of self-sustaining transcription clusters. In contrast, Figure 8D represents an architecturally uncoupled state - 23.3%, 25.7%, and 40.1% of TF gene analogs in adult fibroblasts, neonatal fibroblasts, and B lymphocytes, respectively, were not expressed in any transcription cluster. Lastly, we binned all multi-way contact loci involved in self-sustaining transcription clusters at 100 kb resolution and plotted the interaction frequencies of their decomposed pairwise components (Figure 8E).

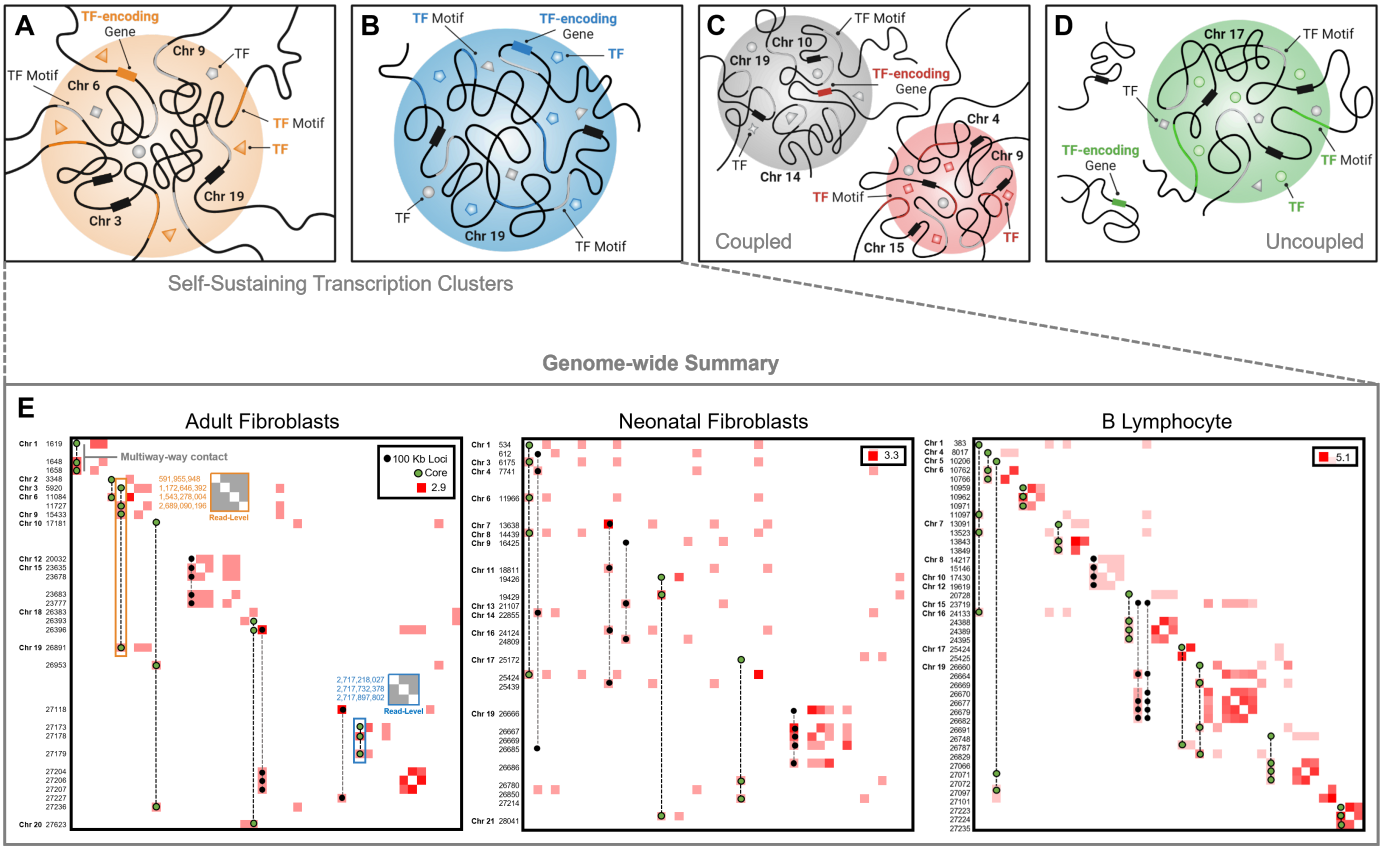

Figure 8: Classes of transcription clusters. In a self-sustaining transcription cluster, a TF and the gene encoding that TF are both present. The inter- and intra-chromosomal examples in (A) and (B), respectively, illustrate this phenomenon where in (A) we see the TF of interest (orange triangle) circulating at the cluster, its binding motif present on the chromatin (orange portion), and its corresponding gene expressed (orange rectangle on Chromosome 6). The gray shapes represent additional TFs with binding motifs (gray portion of chromatin) at the cluster. Black rectangles on Chromosomes 3, 9, and 19 represent additional genes present in the cluster. (C) An analog-independent class of transcription clusters where we observe a TF (red square) bind at a transcription cluster (red cluster) and its corresponding gene expressed in a separate transcription cluster (grey cluster), yet not in the same cluster. (D) An analog-independent class of transcription clusters where we observe a TF (green circle) bind at a transcription cluster (green cluster) and its corresponding gene expressed but not within a transcription cluster. (E) Genome-wide cell type-specific self-sustaining transcription clusters extracted from multi-way contact data and decomposed into Hi-C contact matrices at 100 kb resolution. Contact frequencies are log-transformed for better visualization. Frequencies along the diagonal indicate interaction between two or more unique multi-way loci that fall within the same 100 kb bin. Axis labels are non-contiguous 100 kb bin coordinates in chromosomal order. Multi-way contacts that make up the self-sustaining transcription clusters are superimposed. Multi-way contacts with green-colored loci represent 'core' transcription clusters - transcription clusters containing a master regulator and its gene analog. An example read-level contact map for the inter-chromosomal FOXO3 self-sustaining transcription cluster is denoted by the orange highlighted box in the adult fibroblast contact matrix and a read-level contact map for the intra-chromosomal ZNF320 self-sustaining transcription cluster is denoted by the blue highlighted box. Values along the left axis of these read-level contact matrices are base-pair positions of the contacting loci in the genome.

Order	Multi-way Contacts	Transcription Clusters	Clusters with $\geq$ 1 Gene	Clusters with $\geq$ 2 Genes	Clusters with Common TFs	Clusters with Common MRs
3	240,477	8,384	7,384	4,157	3,788	3,645
	301,366	8,182	7,615	5,208	4,839	4,439
	379,165	11,261	10,581	7,518	6,890	6,778
4	227,352	4,345	3,972	2,686	2,435	2,341
	156,742	2,593	2,467	2,008	1,868	1,729
	181,554	3,254	3,159	2,658	2,515	2,468
5	196,423	1,996	1,881	1,434	1,103	957
	98,172	999	976	834	572	443
	98,272	1,021	999	877	688	614
6+	1,000,231	1,802	1,727	1,419	932	783
	178,705	590	583	549	368	303
	142,575	544	542	514	395	340

Table 1: Summary of multi-way contacts and transcription clusters. Multi-way contacts from B lymphocytes (white rows), neonatal fibroblasts (light gray rows), and adult fibroblasts (dark gray rows, V1-V4) are listed after different filtering criteria. Multi-way contacts are considered to be potential transcription clusters if all loci within the multi-way contact are accessible and at least one locus binds RNA Pol II. These multi-way contacts are then queried for nearby expressed genes. If a transcription cluster candidate has at least two expressed genes, we determine whether the majority of these genes have common transcription factors (TFs) through binding motifs. If only two expressed genes are contained within a transcription cluster candidate, we require both genes to have common TFs. From the set of transcription clusters with common TFs, we calculate how many clusters have at least one common master regulator (MR) (Algorithm 3).

Algorithm 1: Multi-way Contact Analysis

Input: Aligned Pore-C data ($\mathbf{A}$), RNA-seq ($\mathbf{R}$: gene expression), RNA Pol II ($\mathbf{P}$: ChIP-seq), ATAC-seq ($\mathbf{C}$: chromatin accessibility), transcription factor binding motifs ($\mathbf{B}$)
for each set of Pore-C data $\mathbf{A}_l \in \mathbf{A}$ **do**
  Construct incidence matrix $\mathbf{H}_l$ using Algorithm 2
  Identify transcription clusters $\mathbf{T}_{lp}$, $\mathbf{T}_{lc}$, and $\mathbf{T}_{ls}$ using Algorithm 3
  Calculate entropy S_l using Algorithm 4
end for
Compute hypergraph distance d_{ij} between pairs $\mathbf{H}_i$ and $\mathbf{H}_j$ with $p \geq 1$ using Algorithm 5
Calculate the statistical significance α_{ij} for hypergraph distance d_{ij} using the permutation test in Algorithm 6.
Return: Hypergraph incidence matrices $\mathbf{H}_l \in \mathbb{R}^{n \times m}$, hypergraph entropy S_l, potential transcription clusters $\mathbf{T}_{lp}$, transcription clusters $\mathbf{T}_{lc}$, specialized transcription clusters $\mathbf{T}_{ls}$, and hypergraph distance matrix $[d_{ij}]$ with statistical significance $[\alpha_{ij}]$.

3 Discussion

In this work, we introduce a hypergraph framework to study higher-order genome organization from Pore-C long-read sequence data. We demonstrate that higher-order genome architecture can be precisely represented and analyzed using hypergraph theory. Using direct capture of multi-way contacts, we identified transcription clusters with physical proximity and coordinated gene expression. Our framework thus enables study of explicit structure-function relationships that are observed directly from data, without needing to infer multi-way contacts. In engineering and social systems, hypergraph representation of data has revealed higher-order organization principles efficiently [15, 16, 17, 44]. Our work here extends the application of hypergraphs, demonstrating a natural way to represent and analyze genome organization across scales.

Exploring long-range, inter-chromosomal interactions genome-wide offers the opportunity to establish fundamental principles of genome organization. Unbiased capture and study of multi-way contacts can help identify biologically important assemblies that affect transcription, such as transcription clusters [31, 45]. This approach can also connect genome organization principles to the study of transcription factors and how they govern cell type-specific network architecture, which resembles small world phenomena [25, 46]. Our results support the idea of cell type-specific formation of transcription clusters that serve as a basis for efficient navigation of information within the nucleus, and thereby reflect a signature of small world architecture.

Analogous to the behavior of short-path information propagation in social networks, we posit that transcription clusters act as decentralized nodes, or critical architectures relevant to cell identity. Future work to explore these phenomena systematically will undoubtedly help us understand cell type-specific organization principles. Another exciting direction will be to investigate time series multi-way interactions during cellular transitions such as differentiation and cell reprogramming, with single cell observations. Furthermore, we imagine that multi-way chromatin structure together with spatial transcriptomics will guide us to uncover formation principles in tissue patterning and organogenesis [47, 48].

4 Materials and Methods

Cell Culture. Primary human adult dermal fibroblasts were obtained from a donor and were maintained in Dulbecco's Modified Eagle Medium (DMEM) supplemented with 10% fetal bovine serum (FBS), 1X Glutamax (Thermo Fisher Scientific Cat no. 35050061) and 1X nonessential amino acid (Thermo Fisher Scientific Cat no. 11140050).

Cross-linking. Protocols for cross-linking were based on Ulahannan et al. [12]. 2.5 million cells were washed three times in chilled 1X phosphate buffered saline (PBS) in a 50 mL centrifuge tube, pelleted by centrifugation at 500 x g for 5 min at 4°C between each wash. Cells were resuspended in 10 mL room temperature 1X PBS 1% formaldehyde (Fisher Scientific Cat no. BP531-500) by gently pipetting with a wide bore tip, then incubated at room temperature for 10 min. To quench the cross-linking reaction 527 µL of 2.5 M glycine was added to achieve a final concentration of 1% w/v or 125 mM in 10.5 mL. Cells were incubated for 5 min at room temperature followed by 10 min on ice. The cross-linked cells were pelleted by centrifugation at 500 x g for 5 min at 4°C.

Restriction Enzyme Digest. The cell pellet was resuspended in 500 µL of cold permeabilization buffer (10 mM Tris-HCl pH 8.0, 10 mM NaCl, 0.2% IGEPAL CA-630, 100 µL of protease inhibitor cock-tail Roche Cat no. 11836170001) and placed on ice for 15 min. One tablet of protease inhibitor cocktail was dissolved in 1 ml nuclease free water and 100 µL from that was added to a 500 µL permeabilization buffer. Cells were centrifuged at 500 x g for 10 min at 4°C after which the supernatant was aspirated and replaced with 200 µL of chilled 1.5X New England Biolabs (NEB) cutsmart buffer. Cells were centrifuged again at 500 x g for 10 min at 4°C, then aspirated and re-suspended in 300 µL of chilled 1.5X NEB cutsmart buffer. To denature the chromatin, 33.5 µL of 1% w/v sodium dodecyl sulfate (SDS, Invitrogen Cat no. 15553-035) was added to the cell suspension and incubated for exactly 10 min at 65°C with gentle agitation then placed on ice immediately afterwards. To quench the SDS, 37.5 µL of 10% v/v Triton X-100 (Sigma Aldrich Cat no. T8787-250) was added for a final concentration of 1%, followed by incubation for 10 min on ice. Permeabilized cells were then digested with a final concentration of 1 U/µL of NlaIII (NEB-R0125L) and brought to volume with nuclease-free water to achieve a final 1X digestion reaction buffer in 450 µL. Cells were then mixed by gentle inversion. Cell suspensions were incubated in a thermomixer at 37°C for 18 hours with periodic rotation.

Proximity Ligation and Reverse Cross-linking. NlaIII restriction digestion was heat inactivated at 65°C for 20 min. Proximity ligation was set up at room temperature with the addition of the following reagents: 100 µL of 10X T4 DNA ligase buffer (NEB), 10 µL of 10 mg/mL BSA and 50 µL of T4 Ligase (NEB M0202L) in a total volume of 1000 µL with nuclease-free water. The ligation was cooled to 16°C and incubated for 6 hours with gentle rotation.

Protein Degradation and DNA Purification. To reverse cross-link, proximity ligated sample was treated with 100 µL Proteinase K (NEB P8107S-800U/ml), 100 µL 10% SDS (Invitrogen Cat no. 15553-035) and 500 µL 20% v/v Tween-20 (Sigma Aldrich Cat no. P1379) in a total volume of 2000 µL with nuclease-free water. The mixture was incubated in a thermal block at 56°C for 18 hours. In order to purify DNA, the sample was transferred to a 15 mL centrifuge tube, rinsing the original tube with a further 200 µL of nuclease-free water to collect any residual sample, bringing the total sample volume to 2.2 mL. DNA was then purified from the sample using a standard phenol chloroform extraction and ethanol precipitation.

Nanopore Sequencing. Purified DNA was Solid Phase Reversible Immobilization (SPRI) size selected before library preparation with a bead ratio of 0.48X for fragments > 1.5 kb. The > 1.5 kb products were prepared for sequencing using the protocol provided by Oxford Nanopore Technologies. In brief, 1 µg of genomic DNA input was used to generate a sequencing library according to the protocol provided for the SQK-LSK109 kit (Oxford Nanopore Technologies, Oxford Science Park, UK, version GDE_9063_v109_revU_14Aug2019). After the DNA repair, end prep, and adapter ligation steps, SPRI select bead suspension (Cat No. B23318, Beckman Coulter Life Sciences, Indianapolis, IN, USA) was used to remove short fragments and free adapters. A bead ratio of 1X was used for DNA repair and end prep while a bead ratio of 0.4X was used for the adapter ligation step. Qubit dsDNA assay (ThermoFisher Scientific, Waltham, MA, USA) was used to quantify DNA and ∼300-400 ng of DNA library was loaded onto a GridION flow cell (version R9, Flo-MIN 106D). For adult fibroblasts, 4 sequencing runs were conducted generating a total of 6.25 million reads (referred to as V1-V4). For neonatal fibroblasts, 4 sequencing runs were conducted generating a total of 11.85 million reads.

Sequence Processing. Reads which passed Q-score filtering (`--min_qscore 7`, 4.56 million reads) after base calling on the Oxford Nanopore GridION (Guppy, version 4.0.11) were used as input for the Pore-C-Snakemake pipeline (https://github.com/nanoporetech/Pore-C-Snakemake, commit 6b2f762). The pipeline maps multi-way contacts to a reference genome and stores the hyperedge data in a variety of formats. The reference genome used for mapping was GRCh38.p13 (https://www.ncbi.nlm.nih.gov/assembly/GCF_000001405.39/). Each of the four sequencing runs were assigned a sequencing run label and then concatenated. The combined pipeline outputs were used as standard inputs for all downstream analysis.

Hypergraphs. A hypergraph is a generalization of a graph. Hypergraphs are composed of hyperedges, which can join any number of nodes [49]. Mathematically, a hypergraph is a pair such that $\mathsf{G} = \{\mathbf{V}, \mathbf{E}\}$ where $\mathbf{V}$ is the node set and $\mathbf{E}$ is the hyperedge set. Each hyperedge in $\mathbf{E}$ is a subset of $\mathbf{V}$. Examples of hypergraphs include email communication networks, co-authorship networks, film actor/actress networks, and protein-protein interaction networks. For genomic networks, traditional graph-based methods fail to capture contacts that contain more than two genomic loci once, which results in a loss of higher order structural information. Hypergraphs can capture higher order connectivity patterns and represent multidimensional relationships unambiguously in genomic networks [15, 50]. In hypergraphs obtained from Pore-C data, we defined nodes as genomic loci at a particular resolution (e.g. read level, 100 kb, 1 Mb, or 25 Mb bins), and hyperedges as contacts among genomic loci. We switch between these different resolutions both for computational efficiency and visual clarity. Most higher order contacts are unique in Pore-C data at high resolution (read level or 100 kb), so for these data we considered unweighted hypergraphs (i.e. ignore the frequency of contacts). For lower resolutions (1 Mb or 25 Mb), we considered edge weights (frequency of contacts) to find the most common intra- and inter-chromosomal contacts.

Hypergraph Filtering. We performed an additional filtering step while constructing genomic hypergraphs. We first decomposed each multi-way contact into its pairwise combinations at a particular resolution. From these pairwise contacts, we counted the number of times a contact was detected for each pair of loci, and identified the highest frequency locus pairs. Pairwise contacts were kept if they occurred above a certain threshold number, which was set empirically at the 85th percentile of the most frequently occurring locus pairs. For example, in fibroblast data binned at 1 Mb resolution, a locus pair with six detected contacts corresponded to the 85th percentile. Thus all pairs of loci with fewer than six detected contacts were not considered, which increases confidence in the validity of identified multi-way contacts.

Incidence Matrices. An incidence matrix of the genomic hypergraph was an n-by-m matrix containing values zero and one. The row size n was the total number of genomic loci, and the column size m was the total number of unique Pore-C contacts (including self-contacts, pairwise contacts, and higher order contacts). Nonzero elements in a column of the incidence matrix indicate genomic loci contained in the corresponding Pore-C contact. Thus, the number of nonzero elements (or column sum) gives the order of the Pore-C contact. The incidence matrix of the genomic hypergraph can be visualized via PAOHvis [51]. In PAOHvis, genomic loci are parallel horizontal bars, while Pore-C contacts are vertical lines that connect multiple loci (see Figures 1, 2, 3, and 4). Beyond visualization, incidence matrices play a significant role in the mathematical analysis of hypergraphs.

Data-driven Identification of Transcription Clusters. We used Pore-C data in conjunction with multiple other data sources to identify potential transcription clusters (Figure 6). Each locus in a Pore-C read, or multi-way contact, was queried for chromatin accessibility and RNA Pol II binding (ATAC-seq and ChIP-seq peaks, respectively). Multi-way contacts were considered to be potential transcription clusters if all loci within the multi-way contact were accessible and at least one locus had binding of RNA Pol II. The loci in potential transcription clusters were then queried for nearby expressed genes. A 5 kb flanking region was added upstream and downstream of each locus when querying for chromatin accessibility, RNA Pol II binding, and nearby genes [52]. Gene expression (RNA-seq) and transcription factor binding site data were then integrated to determine coexpression and coregulation of genes in potential transcription clusters. If a potential transcription cluster candidate had at least two genes present, and these genes had common transcription factors based on binding motifs in the cluster, the potential transcription cluster was determined to be a real transcription cluster. From the set of transcription clusters with common transcription factors, we calculated how many clusters were regulated by at least one master regulator, a transcription factor that also regulates its own gene, and classified these as specialized transcription clusters (Figure 6).

Transcription Factor Binding Motifs. Transcription factor binding site motifs were obtained from "The Human Transcription Factors" database [53]. FIMO (https://meme-suite.org/meme/tools/fimo) was used to scan for motifs within $\pm$ 5 kb of genes' transcription start sites. The results were converted to a 22,083 $\times$ 1,007 MATLAB table, where rows were genes, columns were transcription factors, and entries were the number of binding sites for a particular transcription factor and gene. The table was then filtered to only include entries with three or more binding sites in downstream computations. This threshold was determined empirically and is adjustable in the MATLAB code.

Identifying Self-Sustaining Transcription Clusters From identified transcription clusters (Table 1), we obtained a subset containing TF-encoding genes specific to each cell type, yielding 79, 54, and 144 transcription clusters from the adult

fibroblast, neonatal fibroblast, and B lymphocyte data, respectively. We then classified these clusters as self-sustaining if the TF binding motif corresponding to the expressed TF-encoding gene was also at the cluster. We further determined whether the self-sustaining TFs were master regulators based on protein-DNA interaction data. Results are summarized in Figure 8 and Table S7.

Public Data Sources. Pore-C data for B lymphocytes were downloaded from Ulahannan *et al.* [12]. ATAC-seq and ChIP-seq data were obtained from the Encyclopedia of DNA Elements (ENCODE) to assess chromatin accessibility and RNA Pol II binding, respectively. These data were compared to read-level Pore-C contacts to determine whether colocalizing loci belong to accessible regions of chromatin and had RNA Pol II binding for both fibroblasts and B lymphocytes. RNA-seq data were also obtained from ENCODE to ensure that genes within potential transcription clusters were expressed in their respective cell types. Additionally, ChIP-seq data for CTCF, RAD21, and SMC3 binding were obtained from ENCODE to evaluate binding preference at transcription clusters. A summary of these data sources can be found in Table 2.

Data Type	Cell Type	Data Description and Source
Pore-C	IR	Human adult primary dermal fibroblasts were derived from a donor skin biopsy
Pore-C	BJ	Human foreskin fibroblasts from BJ cell line (Cat no. CRL-2522, ATCC, Manassas, VA)
Pore-C	GM12878	B lymphocyte Pore-C data obtained from Ulahannan *et al.* [12]
ATAC-seq	IMR-90	Adult fibroblast chromatin accessibility (ENCFF310UDS)
DNase-seq	BJ	Foreskin fibroblast chromatin accessibility (ENCFF310UDS)
ATAC-seq	GM12878	B lymphocyte chromatin accessibility data (ENCFF410XEP)
ChIP-seq	IMR-90	Adult fibroblast RNA Polymerase II binding data (ENCFF676DGR)
ChIP-seq	GM12878	B lymphocyte RNA Polymerase II binding data (ENCFF912DZY)
ChIP-seq	IMR-90	Adult fibroblast CTCF binding data (ENCFF203SRF)
ChIP-seq	BJ	Human foreskin fibroblasts CTCF binding data (ENCFF518RUC)
ChIP-seq	GM12878	B lymphocyte CTCF binding data (ENCFF951PEM)
ChIP-seq	IMR-90	Adult fibroblast RAD21 binding data (ENCSR000EFJ)
ChIP-seq	GM12878	B lymphocyte RAD21 binding data (ENCSR000EAC)
ChIP-seq	IMR-90	Adult fibroblast SMC3 binding data (ENCSR000HPG)
ChIP-seq	GM12878	B lymphocyte SMC3 binding data (ENCSR000DZP)
RNA-seq	IMR-90	Adult fibroblast gene expression data averaged over two replicates (ENCFF353SBP, ENCFF496RIW)
RNA-seq	IR	Adult fibroblast primary gene expression data
RNA-seq	BJ	Neonatal fibroblast gene expression data averaged over two replicates (ENCFF477JDG, ENCFF005WBQ)
RNA-seq	BJ	Foreskin fibroblast primary gene expression data on BJ cell line
RNA-seq	GM12878	B lymphocyte gene expression data averaged over two replicates (ENCFF306TLL, ENCFF418FIT)
Enhancers	IMR-90	Adult fibroblast enhancer location data from EnhancerAtlas 2.0 [54]
Enhancers	BJ	Foreksin fibroblast enhancer location data from EnhancerAtlas 2.0 [54]
Enhancers	GM12878	B lymphocyte enhancer location data from EnhancerAtlas 2.0 [54]

Table 2: Data sources. Data obtained from ENCODE unless otherwise specified [55].

Hypergraph Entropy. Network entropy often is used to measure the connectivity and regularity of a network [17, 56, 57]. We defined a new notion of hypergraph entropy to quantify the organization of chromatin structure from Pore-C data. Denote the incidence matrix of the genomic hypergraph as $\mathbf{H}$. The Laplacian matrix is then an n-by-n matrix (n is the total number of genomic loci in the hypergraph), which can be computed by

$$\mathbf{L} = \mathbf{D} - \mathbf{H}\mathbf{E}^{-1}\mathbf{H}^{\top} \in \mathbb{R}^{n\times n}, \tag{1}$$

where $\mathbf{D} \in \mathbb{R}^{n\times n}$ is a diagonal matrix containing the degrees of nodes along its diagonal, and $\mathbf{E} \in \mathbb{R}^{m\times m}$ is a diagonal matrix containing the orders of hyperedges along its diagonal. Inspired by von Neumann graph entropy (which utilizes the distribution of the eigenvalues from the graph Laplacian matrix), we define the hypergraph entropy as

$$\textbf{Hypergraph Entropy} = -\sum_{i=1}^{n} \bar{\lambda}_i \ln \bar{\lambda}_i, \tag{2}$$

where $\bar{\lambda}_i$ are the normalized eigenvalues of $\mathbf{L}$ such that $\sum_{i=1}^{n} \bar{\lambda}_i = 1$, and the convention $0 \ln 0 = 0$ is used. In mathematics, eigenvalues can quantitatively represent different features of a matrix [58]. Biologically, genomic regions with high entropy

are likely associated with high proportions of euchromatin (i.e. less organized folding patterns), as euchromatin is more structurally permissive than heterochromatin [59, 60, 61].

We computed the entropy of intra-chromosomal genomic hypergraphs for both fibroblasts and B lymphocytes as shown in Table S8. It is expected that larger chromosomes have larger hypergraph entropy because more potential genomic interactions occur in the large chromosomes. However, there are still subtle differences between the fibroblast and B lymphocyte chromosomes, indicating differences in their genome structure. In order to better quantify the structural properties of chromosomes and compare between cell types, it may be useful to introduce normalizations to hypergraph entropy in the future.

Hypergraph Distance. Comparing graphs is a ubiquitous task in data analysis and machine learning [62, 62, 63, 64]. In order to quantify difference between two genomic hypergraphs G_1 and G_2 at different scales, we propose to use several hypergraph distance or similarity measures. These measures are based on conversion of hypergraph into a graph representation, see [44] for details. Denote the incidence matrices of two genomic hypergraphs by $\mathbf{H}_1 \in \mathbb{R}^{n\times m_1}$ and $\mathbf{H}_2 \in \mathbb{R}^{n\times m_2}$, respectively. For $i = 1, 2$, construct the adjacency matrices $\mathbf{A}_i$ and normalized Laplacian matrices $\tilde{\mathbf{L}}_i$:

$$\mathbf{A}_i = \mathbf{H}_i\mathbf{E}_i^{-1}\mathbf{H}_i^\top, \qquad \tilde{\mathbf{L}}_i = \mathbf{I} - \mathbf{D}_i^{-\frac{1}{2}}\mathbf{H}_i\mathbf{E}_i^{-1}\mathbf{H}_i^\top\mathbf{D}_i^{-\frac{1}{2}} \in \mathbb{R}^{n\times n}, \tag{3}$$

respectively, where $\mathbf{I} \in \mathbb{R}^{n\times n}$ is the identity matrix, $\mathbf{E}_i \in \mathbb{R}^{m_i\times m_i}$ is a diagonal matrix containing the orders of hyperedges along its diagonal, and $\mathbf{D}_i \in \mathbb{R}^{n\times n}$ is a diagonal matrix containing the degrees of nodes along its diagonal [65]. The degree of a node is equal to the number of hyperedges that contain that node. Given these adjacency and normalized Laplacian matrices, we use following three distance measures in our application to determine differences in the two genomic hypergraphs at both local and global scales:

- **Hamming Distance:** measures local similarity and is based on absolute values of difference between the two adjacency matrices, i.e.,

$$D_H(\mathsf{G}_1, \mathsf{G}_2) = \frac{1}{n^2}\sum_{j=1}^{n}\sum_{k=1}^{n}|\mathbf{A}_{1,jk} - \mathbf{A}_{2,jk}|,$$

  where, the notation $\mathbf{A}_{i,jk}$ implies jk-th entry of the matrix $\mathbf{A}_i$.

- **Spectral Distance:** measures global similarity and is based on the p-norm for difference between ordered set of eigenvalues of the two Laplacians, i.e.,

$$D_\lambda(\mathsf{G}_1, \mathsf{G}_2) = \frac{1}{n}(\sum_{j=1}^{n}|\lambda_{1,j} - \lambda_{2,j}|^p)^{1/p}, \tag{4}$$

  where $\lambda_{i,j}$ is the jth eigenvalue of $\tilde{\mathbf{L}}_i$ for $i = 1, 2$, and $p \geq 1$. In our analysis, we choose $p = 2$.

- **DeltaCon Distance:** measures both local and global similarity, and is based on the fast belief propagation method of measuring node affinities using the matrix [66],

$$\mathbf{S}_i = \left(\mathbf{I} + \epsilon^2\mathbf{D}_i^a - \epsilon\mathbf{A}_i\right)^{-1},$$

  where, $0 < \epsilon \ll 1$ is small constant capturing the influence between neighboring nodes, and $\mathbf{D}_i^a$ is the $n \times n$ diagonal matrix with the diagonal entries $\mathbf{D}_{i,jj}^a = \sum_{k=1}^{n}\mathbf{A}_{i,jk}$. DeltaCon then compares the two matrices $\mathbf{S}_1$ and $\mathbf{S}_2$ via the Matusita difference as the measure,

$$D_\Delta(\mathsf{G}_1, \mathsf{G}_2) = \frac{1}{n^2}\left(\sum_{j=1}^{n}\sum_{k=1}^{n}({\mathbf{S}_{1,jk}}^{1/2} - {\mathbf{S}_{2,jk}}^{1/2})^2\right)^{1/2}. \tag{5}$$

  where we have added a normalization factor $\frac{1}{n^2}$. In our analysis, we found results too insensitive to the choice of ϵ, and report the results for $\epsilon = 10^{-3}$.

Further details on the properties of these different distances can be found in Supplemental Notes.

We computed hypergraph distance between genome-wide hypergraphs derived from adult fibroblasts, neonatal fibroblasts, and B lymphocytes using the Hamming, spectral, and DeltaCon distances described above and examined distances statistically through a permutation test. Figure S2A1-3 demonstrates that the adult fibroblast and B lymphocyte hypergraphs are significantly different at the chromosome level, especially along Chromosome 21, in stark contrast to the distance between adult and neonatal fibroblasts. Additionally, we computed the same distance measures at the genome level, incorporating inter-chromosomal data, and found that the genomic hypergraphs between fibroblasts and B lymphocytes were significantly different, with a p-value of 0 compared to an observed insignificant difference between adult and neonatal fibroblasts (p-value of 1) S2B1-3.

Statistical Significance via Permutation Test. In order to assess the statistical significance of the transcription cluster candidates we determined using our criteria (Figure 6), we used a permutation test which builds the shape of the null hypothesis (i.e. the random background distribution) by resampling the observed data over N trials. We randomly selected n 3rd, 4th, 5th, and 6th or more order multi-way contacts from our Pore-C data, where n was based on the number of transcription cluster candidates we determined for each order. For example, we randomly selected $n = 11,261$ multi-way contacts from the set of 3rd order multi-way contacts in fibroblasts (Table 1). For each trial, we determined how many of these randomly sampled "transcription clusters" match our remaining criteria: transcription clusters with ≥ 1 gene, ≥ 2 genes, common TFs, and common MRs. The background distribution for each of the criteria was then constructed from these values. The proportion of values in the background distributions that was greater than their counterparts from the data-derived transcription cluster candidates yielded the p-value. This analysis was based on the assumption that transcription clusters will be more likely to contain genes and that those genes are more likely to have common transcription factors than random multi-way contacts. For this analysis, we chose $N = 1,000$ trials.

Similarly, we used a permutation test to determine the significance of the measured distances between two hypergraphs. Suppose that we are comparing two hypergraphs G_1 and G_2. We first randomly generate N hypergraphs $\{\mathsf{R}_i\}_{i=1}^{N}$ that are similar to G_1 ("similar" means similar number of node degree and hyperedge size distribution). The background distribution therefore can be constructed by measuring the hypergraph distances between G_1 and R_i for $i = 1, 2, \ldots, N$. The proportion of distances that was greater than the distance between G_1 and G_2 in this background distribution yielded the p-value. For this analysis, we again chose $N = 1,000$ trials. See Supplemental Notes for details.

5 Code and Data Availability

All data generated within this manuscript and MATLAB code in our computational framework can be provided upon request.

6 Acknowledgements

We thank Professor Peter Cook from the University of Oxford for his guidance on transcription clusters. We thank Professor Gilbert S. Omenn for his helpful discussions on figures. This work is supported in part by the University of Michigan Genome Science Training Program (GSTP) Fellowship funded by NHGRI under Award Number 5T32HG000040-27 to GAD, the Air Force Office of Scientific Research (AFOSR) award FA9550-18-1-0028 to IR and the Defense Advanced Research Projects Agency (DARPA) award 140D6319C0020 and the National Science Foundation (NSF) award 2035827 to iReprogram, LLC.

7 Author Contributions

IR designed research; GAD, SL, CC, SD, SJ, WM, AC, NB, CR, LM and IR performed research; SL, CC, SD, and IR contributed new reagents/analytic tools; GAD, SL, CC, SD, CR, CS, AC, AS and IR analyzed data; and GAD, SL, CC, SD, CS, NB, AS, MW, LM, IR wrote the paper.

8 Competing Interests

SD is an employee of iReprogram, LLC. LM and IR are co-founders of iReprogram, LLC. NB is an employee of Oxford Nanopore Technologies. SL, CC, and IR have submitted a patent application for the computational framework (2115-008250-US-PS1).

References

[1] Erez Lieberman-Aiden, Nynke L Van Berkum, Louise Williams, Maxim Imakaev, Tobias Ragoczy, Agnes Telling, Ido Amit, Bryan R Lajoie, Peter J Sabo, Michael O Dorschner, et al. Comprehensive mapping of long-range interactions reveals folding principles of the human genome. Science, 326(5950):289–293, 2009.

[2] Tom Misteli. The self-organizing genome: Principles of genome architecture and function. Cell, 183:28–45, 2020.

[3] Haiming Chen, Jie Chen, Lindsey A Muir, Scott Ronquist, Walter Meixner, Mats Ljungman, Thomas Ried, Stephen Smale, and Indika Rajapakse. Functional organization of the human 4d nucleome. Proceedings of the National Academy of Sciences, 112(26):8002–8007, 2015.

[4] Ferhat Ay, Thanh H Vu, Michael J Zeitz, Nelle Varoquaux, Jan E Carette, Jean-Philippe Vert, Andrew R Hoffman, and William S Noble. Identifying multi-locus chromatin contacts in human cells using tethered multiple 3c. BMC genomics, 16(1):1–17, 2015.

[5] Pedro Olivares-Chauvet, Zohar Mukamel, Aviezer Lifshitz, Omer Schwartzman, Noa Oded Elkayam, Yaniv Lubling, Gintaras Deikus, Robert P Sebra, and Amos Tanay. Capturing pairwise and multi-way chromosomal conformations using chromosomal walks. Nature, 540(7632):296–300, 2016.

[6] A Marieke Oudelaar, James OJ Davies, Lars LP Hanssen, Jelena M Telenius, Ron Schwessinger, Yu Liu, Jill M Brown, Damien J Downes, Andrea M Chiariello, Simona Bianco, et al. Single-allele chromatin interactions identify regulatory hubs in dynamic compartmentalized domains. Nature genetics, 50(12):1744–1751, 2018.

[7] Lei Liu, Bokai Zhang, and Changbong Hyeon. Extracting multi-way chromatin contacts from hi-c data. PLoS Computational Biology, 17(12):e1009669, 2021.

[8] Emily M Darrow, Miriam H Huntley, Olga Dudchenko, Elena K Stamenova, Neva C Durand, Zhuo Sun, Su-Chen Huang, Adrian L Sanborn, Ido Machol, Muhammad Shamim, et al. Deletion of dxz4 on the human inactive x chromosome alters higher-order genome architecture. Proceedings of the National Academy of Sciences, 113(31):E4504–E4512, 2016.

[9] Robert A Beagrie, Antonio Scialdone, Markus Schueler, Dorothee CA Kraemer, Mita Chotalia, Sheila Q Xie, Mariano Barbieri, Inês de Santiago, Liron-Mark Lavitas, Miguel R Branco, et al. Complex multi-enhancer contacts captured by genome architecture mapping. Nature, 543(7646):519–524, 2017.

[10] Sofia A Quinodoz, Noah Ollikainen, Barbara Tabak, Ali Palla, Jan Marten Schmidt, Elizabeth Detmar, Mason M Lai, Alexander A Shishkin, Prashant Bhat, Yodai Takei, et al. Higher-order inter-chromosomal hubs shape 3d genome organization in the nucleus. Cell, 174(3):744–757, 2018.

[11] Meizhen Zheng, Simon Zhongyuan Tian, Daniel Capurso, Minji Kim, Rahul Maurya, Byoungkoo Lee, Emaly Piecuch, Liang Gong, Jacqueline Jufen Zhu, Zhihui Li, et al. Multiplex chromatin interactions with single-molecule precision. Nature, 566(7745):558–562, 2019.

[12] Netha Ulahannan, Matthew Pendleton, Aditya Deshpande, Stefan Schwenk, Julie M Behr, Xiaoguang Dai, Carly Tyer, Priyesh Rughani, Sarah Kudman, Emily Adney, et al. Nanopore sequencing of dna concatemers reveals higher-order features of chromatin structure. bioRxiv, page 833590, 2019.

[13] Rieke Kempfer and Ana Pombo. Methods for mapping 3d chromosome architecture. Nature Reviews Genetics, 21(4):207–226, 2020.

[14] Amin Allahyar, Carlo Vermeulen, Britta AM Bouwman, Peter HL Krijger, Marjon JAM Verstegen, Geert Geeven, Melissa van Kranenburg, Mark Pieterse, Roy Straver, Judith HI Haarhuis, et al. Enhancer hubs and loop collisions identified from single-allele topologies. Nature genetics, 50(8):1151–1160, 2018.

[15] Austin R Benson, David F Gleich, and Jure Leskovec. Higher-order organization of complex networks. Science, 353(6295):163–166, 2016.

[16] Can Chen, Amit Surana, Anthony M. Bloch, and Indika Rajapakse. Controllability of hypergraphs. IEEE Transactions on Network Science and Engineering, 8(2):1646–1657, 2020.

[17] Can Chen and Indika Rajapakse. Tensor entropy for uniform hypergraphs. IEEE Transactions on Network Science and Engineering, 7(4):2889–2900, 2020.

[18] Ruochi Zhang and Jian Ma. Matcha: Probing multi-way chromatin interaction with hypergraph representation learning. Cell systems, 10(5):397–407, 2020.

[19] Cameron S Osborne, Lyubomira Chakalova, Karen E Brown, David Carter, Alice Horton, Emmanuel Debrand, Beatriz Goyenechea, Jennifer A Mitchell, Susana Lopes, Wolf Reik, et al. Active genes dynamically colocalize to shared sites of ongoing transcription. Nature Genetics, 36(10):1065–1071, 2004.

[20] Cameron S Osborne and Christopher H Eskiw. Where shall we meet? a role for genome organisation and nuclear sub-compartments in mediating interchromosomal interactions. Journal of cellular biochemistry, 104(5):1553–1561, 2008.

[21] Stefan Schoenfelder, Tom Sexton, Lyubomira Chakalova, Nathan F Cope, Alice Horton, Simon Andrews, Sreenivasulu Kurukuti, Jennifer A Mitchell, David Umlauf, Daniela S Dimitrova, et al. Preferential associations between co-regulated genes reveal a transcriptional interactome in erythroid cells. Nature genetics, 42(1):53–61, 2010.

[22] Iris Zhu, Wei Song, Ivan Ovcharenko, and David Landsman. A model of active transcription hubs that unifies the roles of active promoters and enhancers. Nucleic acids research, 49(8):4493–4505, 2021.

[23] Ralph Stadhouders, Guillaume J Filion, and Thomas Graf. Transcription factors and 3d genome conformation in cell-fate decisions. Nature, 569(7756):345–354, 2019.

[24] Duncan J Watts and Steven H Strogatz. Collective dynamics of 'small-world'networks. nature, 393(6684):440–442, 1998.

[25] CA Brackley, Nick Gilbert, Davide Michieletto, Argyris Papantonis, MCF Pereira, PR Cook, and Davide Marenduzzo. Complex small-world regulatory networks emerge from the 3d organisation of the human genome. Nature communications, 12(1):1–14, 2021.

[26] Jesse R Dixon, Siddarth Selvaraj, Feng Yue, Audrey Kim, Yan Li, Yin Shen, Ming Hu, Jun S Liu, and Bing Ren. Topological domains in mammalian genomes identified by analysis of chromatin interactions. Nature, 485(7398):376–380, 2012.

[27] Suhas SP Rao, Miriam H Huntley, Neva C Durand, Elena K Stamenova, Ivan D Bochkov, James T Robinson, Adrian L Sanborn, Ido Machol, Arina D Omer, Eric S Lander, et al. A 3d map of the human genome at kilobase resolution reveals principles of chromatin looping. Cell, 159(7):1665–1680, 2014.

[28] Jie Chen, Alfred O Hero III, and Indika Rajapakse. Spectral identification of topological domains. Bioinformatics, 32(14):2151–2158, 2016.

[29] David M Suter, Nacho Molina, David Gatfield, Kim Schneider, Ueli Schibler, and Felix Naef. Mammalian genes are transcribed with widely different bursting kinetics. Science, 332(6028):472–474, 2011.

[30] Peter R Cook. The organization of replication and transcription. Science, 284(5421):1790–1795, 1999.

[31] Peter R Cook and Davide Marenduzzo. Transcription-driven genome organization: a model for chromosome structure and the regulation of gene expression tested through simulations. Nucleic Acids Research, 46(19):9895–9906, 2018.

[32] Sandy L Klemm, Zohar Shipony, and William J Greenleaf. Chromatin accessibility and the regulatory epigenome. Nature Reviews Genetics, 20(4):207–220, 2019.

[33] Eliezer Calo and Joanna Wysocka. Modification of enhancer chromatin: what, how, and why? Molecular cell, 49(5):825–837, 2013.

[34] François Spitz and Eileen EM Furlong. Transcription factors: from enhancer binding to developmental control. Nature reviews genetics, 13(9):613–626, 2012.

[35] Jennifer E Phillips and Victor G Corces. Ctcf: master weaver of the genome. Cell, 137(7):1194–1211, 2009.

[36] Chin-Tong Ong and Victor G Corces. Ctcf: an architectural protein bridging genome topology and function. Nature Reviews Genetics, 15(4):234–246, 2014.

[37] Kerstin S Wendt, Keisuke Yoshida, Takehiko Itoh, Masashige Bando, Birgit Koch, Erika Schirghuber, Shuichi Tsutsumi, Genta Nagae, Ko Ishihara, Tsuyoshi Mishiro, et al. Cohesin mediates transcriptional insulation by ccctc-binding factor. Nature, 451(7180):796–801, 2008.

[38] Vania Parelho, Suzana Hadjur, Mikhail Spivakov, Marion Leleu, Stephan Sauer, Heather C Gregson, Adam Jarmuz, Claudia Canzonetta, Zoe Webster, Tatyana Nesterova, et al. Cohesins functionally associate with ctcf on mammalian chromosome arms. Cell, 132(3):422–433, 2008.

[39] Elnaz Alipour and John F Marko. Self-organization of domain structures by dna-loop-extruding enzymes. Nucleic acids research, 40(22):11202–11212, 2012.

[40] Judith HI Haarhuis, Robin H van der Weide, Vincent A Blomen, J Omar Yáñez-Cuna, Mario Amendola, Marjon S van Ruiten, Peter HL Krijger, Hans Teunissen, René H Medema, Bas van Steensel, et al. The cohesin release factor wapl restricts chromatin loop extension. Cell, 169(4):693–707, 2017.

[41] Hui C Tsou, Xinhua Lee, Seong Pan Si, and Monica Peacocke. Regulation of retinoic acid receptor expression in dermal fibroblasts. Experimental cell research, 211(1):74–81, 1994.

[42] Christoph Ruschil, Gisela Gabernet, Gildas Lepennetier, Simon Heumos, Miriam Kaminski, Zsuzsanna Hracsko, Martin Irmler, Johannes Beckers, Ulf Ziemann, Sven Nahnsen, et al. Specific induction of double negative b cells during protective and pathogenic immune responses. Frontiers in immunology, page 3304, 2020.

[43] Jingyu Zhang, Hengyu Chen, Ruoyan Li, David A Taft, Guang Yao, Fan Bai, and Jianhua Xing. Spatial clustering and common regulatory elements correlate with coordinated gene expression. PLoS computational biology, 15(3):e1006786, 2019.

[44] Amit Surana, Can Chen, and Indika Rajapakse. Hypergraph dissimilarity measures. arXiv preprint arXiv:2106.08206, 2021.

[45] Indika Rajapakse, Mark Groudine, and Mehran Mesbahi. Dynamics and control of state-dependent networks for probing genomic organization. Proceedings of the National Academy of Sciences, 108(42):17257–17262, 2011.

[46] Steven H Strogatz. Exploring complex networks. nature, 410(6825):268–276, 2001.

[47] Anjali Rao, Dalia Barkley, Gustavo S França, and Itai Yanai. Exploring tissue architecture using spatial transcriptomics. Nature, 596(7871):211–220, 2021.

[48] Charlène Guillot and Thomas Lecuit. Mechanics of epithelial tissue homeostasis and morphogenesis. Science, 340(6137):1185–1189, 2013.

[49] Claude Berge. Hypergraphs: combinatorics of finite sets, volume 45. Elsevier, 1984.

[50] Michael M Wolf, Alicia M Klinvex, and Daniel M Dunlavy. Advantages to modeling relational data using hypergraphs versus graphs. In 2016 IEEE High Performance Extreme Computing Conference (HPEC), pages 1–7. IEEE, 2016.

[51] Paola Valdivia, Paolo Buono, Catherine Plaisant, Nicole Dufournaud, and Jean-Daniel Fekete. Analyzing dynamic hypergraphs with parallel aggregated ordered hypergraph visualization. IEEE transactions on visualization and computer graphics, 27(1):1–13, 2019.

[52] Shane Neph, Andrew B Stergachis, Alex Reynolds, Richard Sandstrom, Elhanan Borenstein, and John A Stamatoyannopoulos. Circuitry and dynamics of human transcription factor regulatory networks. Cell, 150(6):1274–1286, 2012.

[53] Samuel A Lambert, Arttu Jolma, Laura F Campitelli, Pratyush K Das, Yimeng Yin, Mihai Albu, Xiaoting Chen, Jussi Taipale, Timothy R Hughes, and Matthew T Weirauch. The human transcription factors. Cell, 172(4):650–665, 2018.

[54] Tianshun Gao and Jiang Qian. Enhanceratlas 2.0: an updated resource with enhancer annotation in 586 tissue/cell types across nine species. Nucleic Acids Research, 48(D1):D58–D64, 2020.

[55] ENCODE Project Consortium et al. An integrated encyclopedia of dna elements in the human genome. Nature, 489(7414):57, 2012.

[56] Filippo Passerini and Simone Severini. The von neumann entropy of networks. arXiv:0812.2597, 2008.

[57] Giorgia Minello, Luca Rossi, and Andrea Torsello. On the von neumann entropy of graphs. Journal of Complex Networks, 7(4):491–514, 2019.

[58] Gilbert Strang. Introduction to linear algebra, volume 3. Wellesley-Cambridge Press Wellesley, MA, 1993.

[59] Ben D MacArthur and Ihor R Lemischka. Statistical mechanics of pluripotency. Cell, 154(3):484–489, 2013.

[60] Indika Rajapakse, Mark Groudine, and Mehran Mesbahi. What can systems theory of networks offer to biology? PLoS Computational Biology, 8(6):e1002543, 2012.

[61] Stephen Lindsly, Can Chen, Sijia Liu, Scott Ronquist, Samuel Dilworth, Michael Perlman, and Indika Rajapakse. 4dnvestigator: time series genomic data analysis toolbox. Nucleus, 12(1):58–64, 2021.

[62] Claire Donnat and Susan Holmes. Tracking network dynamics: A survey using graph distances. The Annals of Applied Statistics, 12(2):971 – 1012, 2018.

[63] Katherine Faust and John Skvoretz. Comparing networks across space and time, size and species. Sociological Methodology, 32(1):267–299, 2002.

[64] Peter Wills and François G Meyer. Metrics for graph comparison: a practitioner's guide. PloS One, 15(2):e0228728, 2020.

[65] Dengyong Zhou, Jiayuan Huang, and Bernhard Schölkopf. Learning with hypergraphs: Clustering, classification, and embedding. Advances in Neural Information Processing Systems, 19:1601–1608, 2006.

[66] Danai Koutra, Joshua T Vogelstein, and Christos Faloutsos. Deltacon: A principled massive-graph similarity function. In Proceedings of the 2013 SIAM international conference on data mining, pages 162–170. SIAM, 2013.

[67] Fan R. K. Chung and Fan Chung Graham. Spectral graph theory. Number 92. American Mathematical Soc., 1997.

[68] Sinan G Aksoy, Cliff Joslyn, Carlos Ortiz Marrero, Brenda Praggastis, and Emilie Purvine. Hypernetwork science via high-order hypergraph walks. EPJ Data Science, 9(1):16, 2020.

9 Supplementary Materials

Algorithm 2: Hypergraph incidence matrix construction

Input: Aligned Pore-C data
for each multi-way contact j **do**
  if multi-way contact contains locus i **then**
    $\mathbf{H}(i, j) = 1$
  else
    $\mathbf{H}(i, j) = 0$
  end if
end for
Return: Hypergraph incidence matrix $\mathbf{H} \in \mathbb{R}^{n \times m}$ where n is the total number of loci, and m is the total number of multi-way contacts.

Algorithm 3: Identification of Transcription Clusters

Input: Hypergraph incidence matrix $\mathbf{H}$, gene expression $\mathbf{R}$ (RNA-seq), RNA Pol II $\mathbf{P}$ (ChIP-seq), chromatin accessibility $\mathbf{C}$ (ATAC-seq), transcription factor binding motifs $\mathbf{B}$
for each multi-way contact j in $\mathbf{H}$ **do**
  if all loci are accessible from $\mathbf{C}$ and ≥ 1 locus has Pol II binding from $\mathbf{P}$ **then**
    multi-way contact j from $\mathbf{H}$ is added to the set of potential transcription clusters $\mathbf{T}_p$
  end if
end for
for each potential transcription cluster k in $\mathbf{T}_p$ **do**
  if loci contain ≥ 2 expressed genes from $\mathbf{R}$ and the majority of these genes have ≥ 1 common TFs from $\mathbf{B}$ **then**
    multi-way contact k from $\mathbf{T}_p$ is added to the set of transcription clusters $\mathbf{T}_c$
  end if
  if loci contain ≥ 2 expressed genes from $\mathbf{R}$ and the majority of these genes have ≥ 1 common MRs from $\mathbf{B}$ **then**
    multi-way contact k from $\mathbf{T}_p$ is added to the set of transcription clusters $\mathbf{T}_s$
  end if
end for
Return: Potential transcription clusters $\mathbf{T}_p$, transcription clusters $\mathbf{T}_c$, and specialized transcription clusters $\mathbf{T}_s$

Algorithm 4: Hypergraph Entropy

Input: Hypergraph incidence matrix $\mathbf{H} \in \mathbb{R}^{n \times m}$
Construct the hypergraph Laplacian matrix $\mathbf{L} = \mathbf{D} - \mathbf{H}\mathbf{E}^{-1}\mathbf{H}^{\top} \in \mathbb{R}^{n \times n}$ where $\mathbf{D} \in \mathbb{R}^{n \times n}$ is a diagonal matrix containing the degrees of nodes along its diagonal, and $\mathbf{E} \in \mathbb{R}^{m \times m}$ is a diagonal matrix containing the orders of hyperedges along its diagonal
Compute the eigenvalues λ_i of $\mathbf{L}$ using eigendecomposition
Normalize the eigenvalues $\bar{\lambda}_j = \frac{\lambda_j}{\sum_{i=1}^{n} \lambda_i}$
Compute the hypergraph entropy

$$S = -\sum_j \bar{\lambda}_j \ln \bar{\lambda}_j$$

Return: Hypergraph entropy S.

Algorithm 5: Comparing Hypergraphs

Input: Two hypergraph G_1 and G_2 with incidence matrices $\mathbf{H}_1 \in \mathbb{R}^{n \times m_1}$ and $\mathbf{H}_2 \in \mathbb{R}^{n \times m_2}$

Construct the normalized hypergraph Laplacian matrices

$$\tilde{\mathbf{L}}_i = \mathbf{I} - \mathbf{D}_i^{-\frac{1}{2}} \mathbf{H}_i \mathbf{E}_i^{-1} \mathbf{H}_i^\top \mathbf{D}_i^{-\frac{1}{2}} \in \mathbb{R}^{n \times n},$$

where $\mathbf{I} \in \mathbb{R}^{n \times n}$ is the identity matrix, $\mathbf{E}_i \in \mathbb{R}^{m_i \times m_i}$ is a diagonal matrix containing the orders of hyperedges along its diagonal, and $\mathbf{D}_i \in \mathbb{R}^{n \times n}$ is a diagonal matrix containing the degrees of nodes along its diagonal, for $i = 1, 2$ [65].

Compute the hypergraph distance

$$d = \frac{1}{n} \left(\sum_{i=1}^{n} |\lambda_{1j} - \lambda_{2j}|^p \right)^{\frac{1}{p}},$$

where λ_{ij} is the jth eigenvalue of $\tilde{\mathbf{L}}_i$ for $i = 1, 2$, and $p \geq 1$.

Other options: Hamming distance and DeltaCon distance (see *Materials and Methods*)

Return: Hypergraph distance d between G_1 and G_2.

Algorithm 6: Permutation Test for Hypergraph Distance

Input: Two hypergraph G_1 and G_2, a prescribed significant level α

Null hypothesis H_0: G_1 and G_2 are similar, and alternative hypothesis H_1: G_1 and G_2 are dissimilar

Randomly generate N number of hypergraph $\{\mathsf{R}_i\}_{i=1}^N$ that are similar to G_1 ("similar" means similar number of node degree and hyperedge size distribution)

Construct the the background distribution by measuring the hypergraph distances between G_1 and R_i for $i = 1, 2, \ldots, N$

Compute the actual hypergraph distance between G_1 and G_2

Obtain the p-value by calculating the proportion of distances that are greater than the actual distance in the background distribution

if p-value $\leq \alpha$ **then**

  Reject the null hypothesis H_0

end if

Return: Permutation test result of whether G_1 and G_2 are similar or dissimilar.

Algorithm 7: Identification of Transcription Clusters with Enhancers

Input: Hypergraph incidence matrix $\mathbf{H}$, gene expression $\mathbf{R}$ (RNA-seq), RNA Pol II $\mathbf{P}$ (ChIP-seq), chromatin accessibility $\mathbf{C}$ (ATAC-seq), enhancer locations $\mathbf{E}$, transcription factor binding motifs $\mathbf{B}$

for each multi-way contact j in $\mathbf{H}$ **do**

  if all loci are accessible from $\mathbf{C}$ and ≥ 1 locus has Pol II binding from $\mathbf{P}$ **then**

    multi-way contact j from $\mathbf{H}$ is added to the set of potential transcription clusters $\mathbf{T}_p$

  end if

end for

for each potential transcription cluster k in $\mathbf{T}_p$ **do**

  if loci contain ≥ 2 expressed genes from $\mathbf{R}$ which have ≥ 1 common TFs from $\mathbf{B}$ and ≥ 1 enhancer from $\mathbf{E}$ **then**

    multi-way contact k from $\mathbf{T}_p$ is added to the set of transcription clusters $\mathbf{T}_c$

  end if

  if loci contain ≥ 2 expressed genes from $\mathbf{R}$ which have ≥ 1 common MRs from $\mathbf{B}$ and ≥ 1 enhancer from $\mathbf{E}$ **then**

    multi-way contact k from $\mathbf{T}_p$ is added to the set of transcription clusters $\mathbf{T}_s$

  end if

end for

Return: Potential transcription clusters $\mathbf{T}_p$, transcription clusters $\mathbf{T}_c$, and specialized transcription clusters $\mathbf{T}_s$

10 Supplementary Notes

Hypergraph Distance Measures (HDMs). The Hamming distance compares the neighborhood of each node, i.e. direct neighbours, and thus is a local similarity measure. The spectral distance measures differences in the graph structure at a global scale as it is based on eigenvalues of the normalized Laplacian $\tilde{\mathbf{L}}$ which captures global connectivity patterns within the graph such as community structure, number of spanning trees, etc. [67, 62]. We used normalized Laplacian as its eigenvalues are bounded in the range $[0, 2]$, and thus makes it a more stable and preferable representation [62]. Also, note that while spectral distance is permutation invariant (i.e. invariant to ordering of nodes), Hamming distance and DeltaCon distance

preserve node identities. Consequently, the spectral distance between two isomorphic graphs is zero, and thus not best suited for applications where we want to preserve node (i.e., genomic loci) identities. However, because it captures differences in global connectivity patterns, it can still be useful and we include it in our analysis. The fast belief propagation matrix used in DeltaCon distance is designed to model the diffusion of information throughout a graph [66]. The entry $S_{i,jk}$ of the matrix $\mathbf{S}_i$ indicates the influence that node j has on node k. Intuitively, node j has more influence/affinity to node k if there are many, short heavily-weighted paths from node j to k. Thus, DeltaCon, while preserving node identities, captures differences in global connectivity patterns (in terms of how information flows between any two nodes) in the graphs, and thereby attempts to capture both local and global structural differences.

Permutation Test for HDM. In order to assess statistical significance while comparing two hypergraphs G_1 and G_2 using hypergraph distance, we pose it as a hypothesis testing problem [44], with:

- Null (H_0): G_1 and G_2 are similar,
- Alternative (H_1): G_1 and G_2 are dissimilar.

Since the null distribution for H_0 is unknown, we use a permutation test to empirically estimate it. Let D be any hypergraph distance, and let $0 < p_s < 1$ be the desired significance level of the test. The steps in the permutation test involve:

- Step 1: Randomly generate a family of hypergraphs $\{\mathsf{R}_i\}_{i=1}^N$ which are similar to G_1, and compute $\tilde{D}_i = D(\mathsf{G}_1, \mathsf{R}_i), i = 1, \cdots, N$.
- Step 2: Compute $D_{12} = D(\mathsf{G}_1, \mathsf{G}_2)$.
- Step 3: Compute p-value as $p = \frac{1}{N}\sum_{i=1}^N \mathcal{I}_{D_{12}}(\tilde{D}_i)$, where $\mathcal{I}$ is indicator function, with $\mathcal{I}_z(x) = 1$ if $x > z$ and $\mathcal{I}_z(x) = 0$ otherwise.
- Step 4: Reject H_0 if $p \leq p_s$.

In Step 1, we follow a Chung–Lu (CL) procedure described in [68] to generate R_i with similar vertex degree and edge size distribution as of G_1. Let $d_{1v} = (d(v_1), \cdots, d(v_n))$ and $d_{1e} = (d(e_1), \cdots, d(e_{m_1}))$ be vertex degree and edge size distribution vectors of $\mathsf{G}_1 = (\mathbf{V}_1, \mathbf{E}_1)$, where, $d(v_i)$ is degree of node $v_i \in \mathbf{V}_1$ $i = 1, \cdots, n$ and $d(e_j)$ is order of edge $e_j \in \mathbf{E}_1, j = 1, \cdots, m_1$. In order to be realizable by a hypergraph, vertex degree and edge size distribution should satisfy $c = \sum_{i=1}^n d(v_i) = \sum_{i=1}^{m_1} d(e_i)$. As per this procedure, the probability that a vertex belongs to a hyperedge in R is proportional to the product of the desired vertex degree and edge size, i.e.

$$\mathcal{P}(u \in e) = \frac{d(u)d(e)}{c}$$

To ensure this probability is always less than 1, one may further require that the input sequences satisfy $\max_{i,j} d(u_i)d(e_j) \leq c$.

11 Supplementary Figures

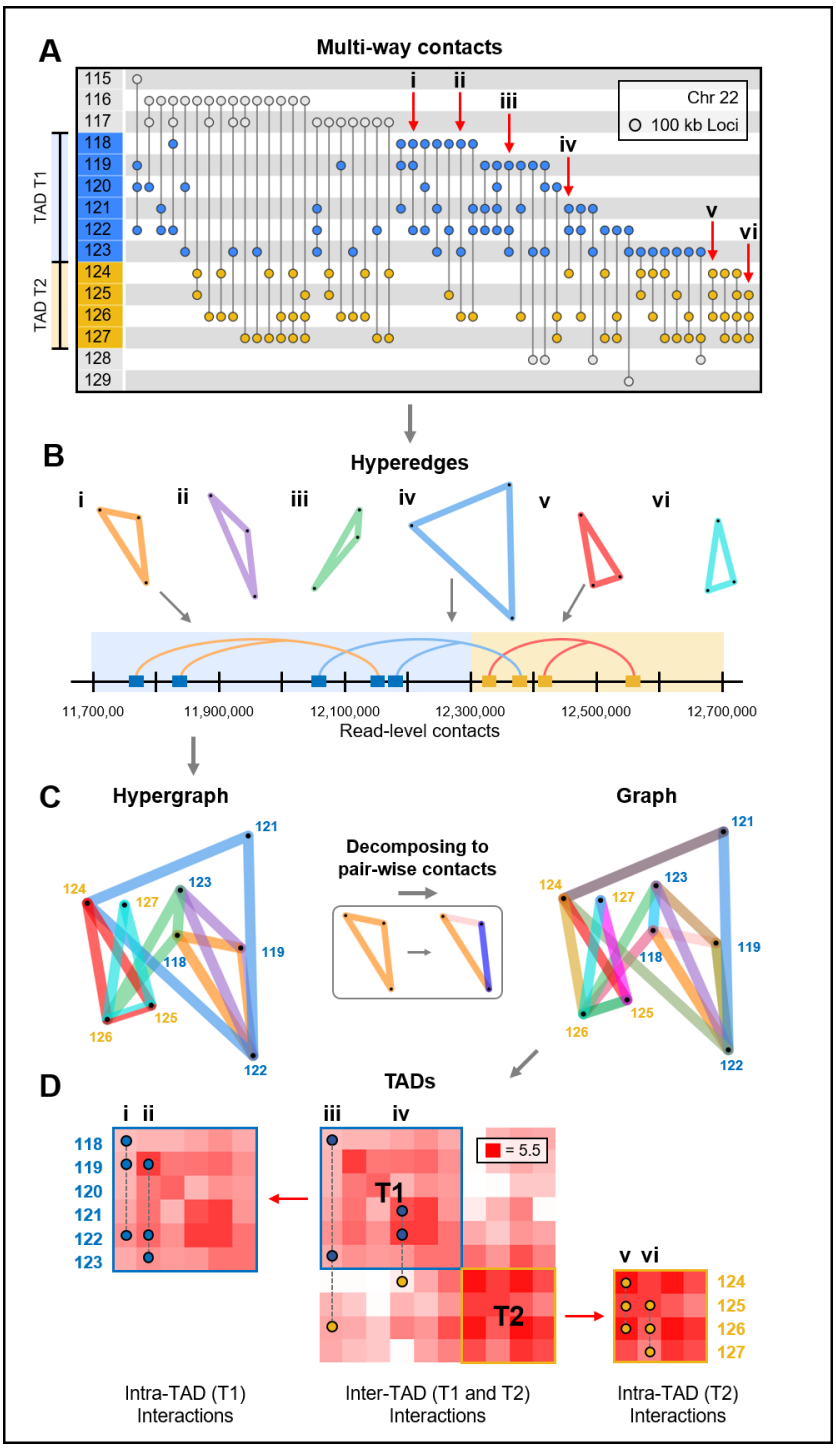

Figure S1: Local organization of the genome. (A) Incidence matrix visualization of a region in Chromosome 22 from B lymphocytes. The numbers in the left column represent genomic loci, vertical lines represent multi-way contacts, where nodes indicate the corresponding locus' participation in this contact. The blue and yellow regions represent two TADs, T1 and T2. The six contacts, denoted by the labels i-vi, are used as examples for hypergraph and genomic folding pattern visualizations. (B) Hypergraph visualization of the multi-way contacts i-vi from A. Blue and yellow labels indicate which TADs these loci participate in. (C) Contact frequency matrices were constructed by separating all multi-way contacts within and between the two TADs into their pairwise combinations. Example multi-way contacts are superimposed onto contact frequency matrices. All multi-way contacts in this figure were determined in 100 kb resolution after noise reduction (*Materials and Methods*).

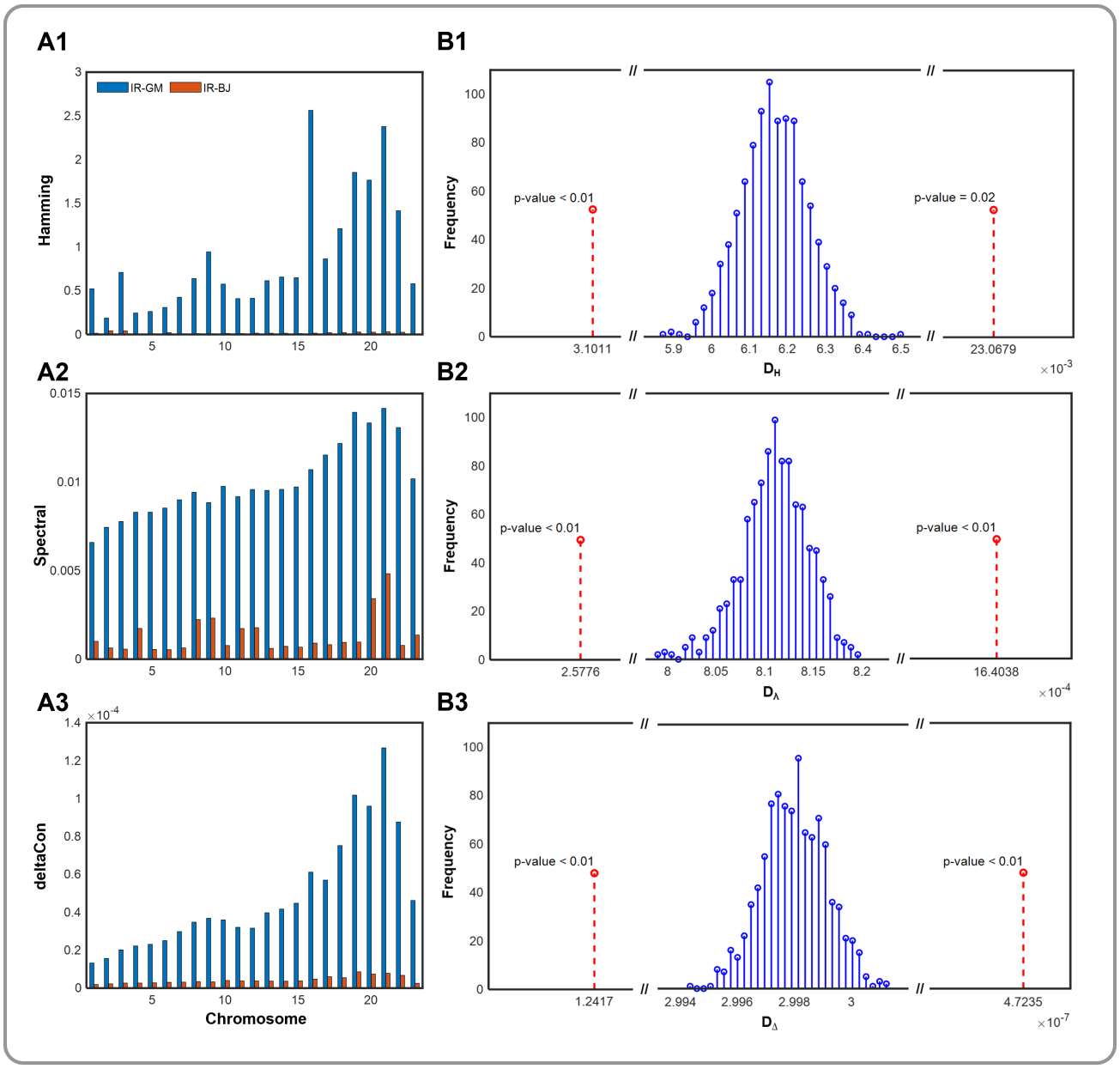

Figure S2: Hypergraph distance between genome-wide hypergraphs derived from adult fibroblasts, neonatal fibroblasts, and B lymphocytes. (A1-3) Hypergraph distance measures computed at the chromosome level between adult fibroblasts and B lymphocytes (blue) and between adult and neonatal fibroblasts (orange). (B1-3) Null distribution formed by measuring the hypergraph distances between the hypergraph derived from adult fibroblasts and random hypergraphs The actual distance between the adult fibroblast and neonatal fibroblast (left) as well as adult fibroblast and B lymphocyte (right) genome-wide hypergraphs is highlighted in red with p-values denoted. IR = adult fibroblasts; BJ = neonatal fibroblasts; GM = B lymphocytes.

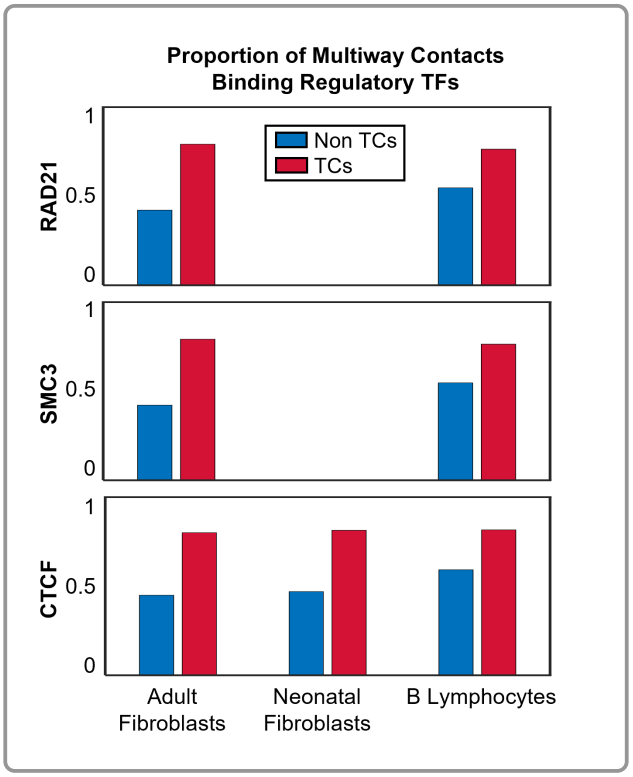

Figure S3: Multi-way contacts with regulatory TF binding. CTCF, a common transcription factor responsible for regulating transcription and chromatin folding, and associated cohesin subunits - RAD21 and SMC3 - all exhibited preferential binding to transcription clusters (TCs) across cell types rather than multi-way contacts not classified as transcription clusters (non TCs). RAD21 and SMC3 ChIP-seq data for the BJ cell line (neonatal fibroblasts) was not available.

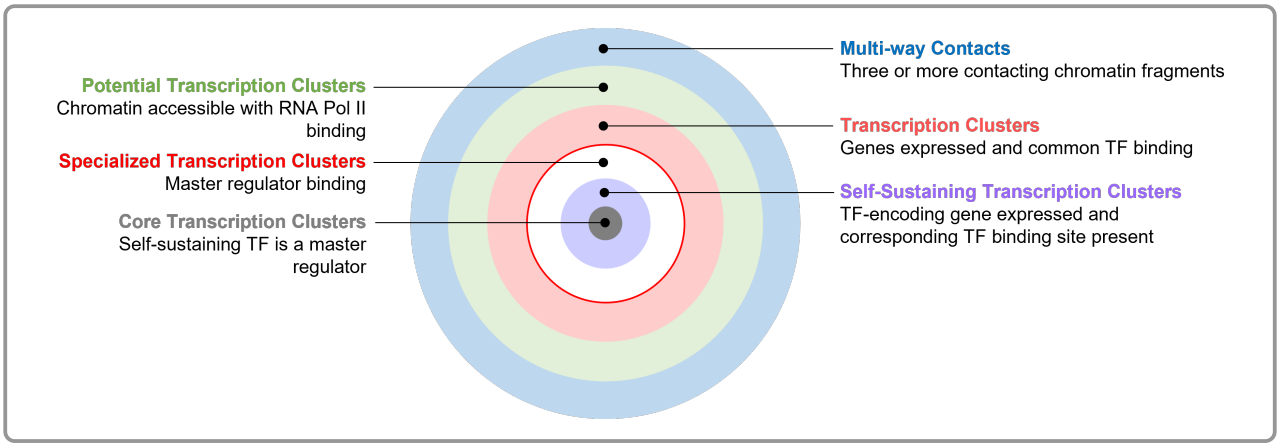

Figure S4: Overview of multi-way contact classifications.

12 Supplementary Tables

File Type	Description
.fastq	Text file which contains unique identifiers for Pore-C reads and the raw sequences contained within each read
.pairs	Text file which contains pairs of aligned genomic loci at base-pair resolution, which can be grouped together using unique identifiers to construct multi-way contacts
.parquet	Text file which contains aligned multi-way contacts at base-pair resolution, restriction fragment assignments, and indicators for the quality of read alignment
.mcool	Binary storage file which contains pairwise interactions from Pore-C data at multiple resolutions

Table S1: Descriptions of file types used within the computational framework (Figure 1).

Order	Multi-way Contacts	Transcription Clusters	Clusters with $\geq$ 2 Genes	Clusters with $\geq$ 1 Enhancer	Clusters with Common TFs	Clusters with Common MRs
3	240,477	8,384	4,157	3,487	3,179	3,063
	301,366	8,182	7,518	358	336	333
	379,165	11,261	7,518	7,358	6,742	6,598
4	227,352	4,345	2,686	2,387	2,172	2,088
	156,742	2,593	2,008	163	150	148
	181,554	3,254	2,658	2,638	2,495	2,443
5	196,423	1,996	1,434	1,315	1,015	885
	98,172	999	834	358	336	333
	98,272	1,021	877	869	672	587
6+	1,000,231	1,802	1,419	1,343	892	757
	178,705	590	549	68	61	59
	142,575	544	514	513	385	336

Table S2: Summary of multi-way contacts with enhancers. Multi-way contacts from B lymphocytes (white rows), neonatal fibroblasts (light gray rows), and adult fibroblasts (dark gray rows, V1-V4) are listed after different filtering criteria. Multi-way contacts are considered to be potential transcription clusters if all loci within the multi-way contact are accessible and at least one locus has binding from RNA Pol II. These multi-way contacts are then queried for nearby expressed genes and enhancers. If a transcription cluster candidate has at least two expressed genes and at least one enhancer locus, we determine whether the majority of these genes have common transcription factors (TFs) through binding motifs. If only two expressed genes are contained within a transcription cluster candidate, we require both genes to have common TFs. From the set of transcription clusters with common TFs, we calculate how many clusters have at least one common master regulator (MR) (Algorithm 7).

Chr	1	2	3	4	5	6	7	8	9	10+
1	230	8,333	14,492	5,501	2,093	872	353	133	54	57
2	241	9,183	15,548	6,180	2,373	873	437	197	71	95
3	198	7,113	13,631	5,113	1,909	750	302	132	57	50
4	190	6,342	11,147	4,360	1,642	598	284	113	56	28
5	179	5,785	10,059	3,897	1,457	640	249	106	39	31
6	167	5,361	9,368	3,551	1,364	511	207	75	39	27
7	159	4,851	8,365	3,258	1,274	453	180	72	35	26
8	143	4,321	7,596	2,864	1,069	393	154	71	32	16
9	122	2,722	4,899	1,831	614	209	76	31	8	6
10	134	4,010	7,185	2,695	912	337	144	63	23	14
11	133	3,698	6,613	2,533	890	330	101	62	14	14
12	132	3,815	6,630	2,497	878	324	114	47	17	12
13	97	2,627	4,767	1,751	588	247	82	37	11	8
14	87	2,209	3,932	1,366	509	140	51	19	10	2
15	82	1,623	2,812	991	298	98	29	16	2	1
16	80	1,650	3,126	1,181	363	127	39	11	5	2
17	82	1,345	2,374	732	201	66	20	4	3	2
18	77	1,828	3,230	1,128	368	149	51	16	10	4
19	56	873	1,455	462	118	41	7	3	0	0
20	64	1,247	2,238	783	222	69	27	6	3	0
21	39	453	809	264	79	18	6	1	0	0
22	39	438	728	206	43	13	3	0	1	0
X	151	1,078	1,852	882	350	119	43	17	10	0
Y	23	70	93	25	6	4	0	0	0	0

Table S3: Adult fibroblast intra-chromosome contact orders (1 Mb resolution).

Chr	1	2	3	4	5	6	7	8	9	10+
1	232	4,725	17,254	16,396	10,752	6,836	4,248	2,663	1,652	3,130
2	243	4,964	16,695	16,702	11,787	7,891	5,172	3,432	2,288	4,631
3	199	4,055	16,351	14,795	9,846	6,376	4,023	2,691	1,759	3,293
4	191	3,725	13,399	13,309	9,192	6,218	4,081	2,632	1,698	3,301
5	180	3,449	12,352	12,458	8,799	5,810	3,672	2,358	1,548	2,728
6	171	3,300	11,249	11,640	7,862	5,307	3,235	2,139	1,376	2,486
7	160	3,086	11,350	11,272	7,758	5,101	3,223	2,213	1,391	2,613
8	145	2,895	10,755	10,608	7,333	4,778	3,141	2,068	1,289	2,477
9	124	2,399	9,360	8,535	5,847	3,802	2,393	1,572	931	1,753
10	134	2,580	9,429	9,273	6,203	4,113	2,576	1,632	1,020	1,856
11	134	2,505	8,979	8,661	5,795	3,629	2,250	1,408	852	1,530
12	134	2,376	8,329	8,200	5,465	3,449	2,192	1,344	833	1,304
13	99	1,763	6,665	6,527	4,585	2,935	1,834	1,078	635	1,159
14	89	1,531	5,909	5,884	3,863	2,236	1,430	858	514	843
15	85	1,349	5,064	5,130	3,354	1,964	1,164	706	372	582
16	83	1,444	5,993	5,722	3,769	2,437	1,419	808	494	813
17	84	1,355	4,278	4,294	2,612	1,514	882	475	271	366
18	80	1,478	6,015	5,569	3,616	2,359	1,380	861	549	840
19	57	884	3,335	3,251	1,998	1,141	664	383	224	252
20	65	1,053	4,344	4,149	2,684	1,656	902	547	315	441
21	40	481	2,285	2,245	1,392	747	402	235	96	127
22	39	445	1,739	1,795	1,098	512	255	127	59	72
X	156	3,681	12,552	11,686	8,206	5,915	3,941	2,738	1,950	4,414

Table S4: GM12878 intra-chromosome contact orders (1 Mb resolution).

Chr	**1**	**2**	**3**	**4**	**5**	**6**	**7**	**8**	**9**	**10+**
1	230	8,112	12,567	5,543	2,385	1,008	442	184	81	52
2	241	9,312	14,641	6,579	3,000	1,316	594	266	106	73
3	197	7,494	11,813	5,199	2,333	978	423	167	76	53
4	190	6,946	10,900	4,973	2,205	924	363	131	60	48
5	179	6,084	9,605	4,397	1,904	772	315	116	57	29
6	166	5,676	9,083	3,992	1,648	647	270	108	41	29
7	159	5,044	8,005	3,582	1526	619	265	101	40	27
8	143	4,538	7,273	3,218	1,339	499	219	82	38	21
9	123	2,746	4,622	2,048	742	275	98	48	7	4
10	134	3,989	6,336	2,894	1,148	507	144	64	29	10
11	134	3,846	6,275	2,758	1,045	414	169	71	18	22
12	133	3,825	6,138	2,622	1,063	422	153	54	15	12
13	97	2,861	4,844	2,097	803	322	114	41	14	1
14	87	2,308	3,816	1,609	595	217	77	26	11	6
15	80	1,566	2,575	980	334	99	34	7	4	0
16	80	1,523	2,859	1,221	444	118	48	16	8	2
17	80	1,237	2,111	767	227	76	28	5	1	0
18	77	1,905	3,332	1,433	509	147	56	19	2	2
19	56	783	1,197	407	122	37	9	3	1	0
20	64	1,277	2,179	884	319	96	34	10	0	2
21	39	482	887	347	100	30	6	1	1	0
22	39	436	706	219	49	8	5	1	0	0
X	151	1,475	2,486	1,231	454	203	80	25	9	6
Y	23	89	137	37	9	2	0	0	0	0

Table S5: Neonatal fibroblast intra-chromosome contact orders (1 Mb resolution).

Neonatal Fibroblast		Adult Fibroblast		B Lymphocyte	
ZNF2	37.2%	**ZNF2**	36.2%	**HINFP**	34.1%
SP2	36.6%	**ZNF441**	35.6%	**ZNF441**	28.7%
HINFP	35.5%	**HINFP**	34.4%	**DNMT1**	28.4%
ZNF441	34.7%	**MBD2**	33.8%	**MBD2**	26.7%
MBD2	34.1%	**ZNF486**	32.3%	**KLF7**	26.3%
TCFL5	33.0%	**TCFL5**	32.1%	**ZNF141**	25.9%
ZNF486	31.6%	**DNMT1**	31.4%	**EGR2**	25.4%
DNMT1	30.9%	**HES1**	30.2%	**ZNF200**	23.8%
HES1	30.6%	**HES4**	30.2%	**CXXC1**	23.6%
HES4	30.6%	**EGR1**	30.2%	**ZNF383**	22.4%
ZNF202	29.3%	**ZNF202**	29.0%	**ZBTB14**	22.3%
EGR1	29.3%	**ZBTB14**	28.5%	**TCFL5**	21.9%
ZBTB14	28.6%	**ZNF200**	28.3%	**ZNF100**	21.7%
KLF7	27.9%	**EGR2**	28.0%	**ZNF202**	21.5%
ZNF200	27.8%	**KLF7**	28.0%	**E2F6**	20.6%

Table S6: Top 15 most frequently observed TF binding sites across transcription clusters.

	Transcription Cluster (Chromosomes)	Gene/TF Analog	Master Regulator?
Adult Fibroblasts	[9 19 3 6]	FOXO3	Y
	[19 19 19]	ZNF134	Y
	[1 1 1]	PBX1	Y
	[18 20 18]	MBD2	Y
	[19 10 19]	[MZF1,ZNF33A]	Y
	[6 2 6]	ATOH8	Y
	[19 18 19 19 18]	TCF4	N
	[19 19 19]	ZNF320	N
	[15 15 15 15 12]	ZNF740	N
Neonatal Fibroblasts	[19 17 19]	ZNF582	Y
	[17 17 17]	STAT3	Y
	[11 11 21]	ETS1	Y
	[6 3 17 1 8]	STAT3	Y
	[19 19 19 19 19]	TCF3	N
	[9 16 13]	ZNF821	N
	[16 7 11 7 17]	ZNF263	N
	[19 1 4 14]	NFIA	N
B Lymphocytes	[16 16 16 12]	MAZ	Y
	[7 16 1 6]	TFAP4	Y
	[19 19 5 19]	ZNF296	Y
	[19 19 19]	ZNF543	Y
	[7 7 7 7]	ZNF783	Y
	[19 19 19 19]	ZBTB7A	Y
	[6 6 4]	HIVEP1	Y
	[19 19 19 19]	ZNF574	Y
	[6 6 6]	ZBTB12	Y
	[17 17 19]	STAT3	Y
	[10 8 8 12]	EGR2	N
	[15 19 19 19 19]	ZNF555	N
	[19 19 15 19 19 19]	ZNF555	N

Table S7: Self-Sustaining Transcription Clusters. All transcription clusters where a TF (specifically its binding motif) and its corresponding TF-encoding gene are both found. The 'Transcription Cluster' column contains the multi-way contacts within and/or between chromosomes that make up the transcription clusters. The 'Gene/TF' column contains the shared TF and TF-encoding gene name. The 'Master Regulator' column denotes whether the TF in the previous column is a master regulator.

Chromosome	**IR**	**BJ**	**GM**
1	5.4289	5.4327	5.4337
2	5.4800	5.4799	5.4808
3	5.2788	5.2783	5.2809
4	5.2308	5.2409	5.2386
5	5.1760	5.1756	5.1784
6	5.1065	5.1064	5.1272
7	5.0568	5.0566	5.0607
8	4.9497	4.9639	4.9689
9	4.7871	4.8037	4.8118
10	4.8846	4.8842	4.8823
11	4.8767	4.8837	4.8964
12	4.8769	4.8839	4.8808
13	4.5591	4.5589	4.5778
14	4.4490	4.4486	4.4698
15	4.3736	4.3729	4.4219
16	4.3747	4.3734	4.4116
17	4.3847	4.3832	4.4085
18	4.3245	4.3246	4.3757
19	4.0167	4.0154	4.0182
20	4.1367	4.1521	4.1517
21	3.6277	3.6548	3.6573
22	3.6268	3.6272	3.6307
X	4.9887	4.9923	5.0380
Whole Genome	**7.9744**	**7.9762**	**7.9784**

Table S8: Hypergraph Entropy. Chromosome-level genomic hypergraphs for adult fibroblasts (IR), neonatal fibroblasts (BJ) and B lymphocytes (GM). Last row is the genome-wide hypergraph entropy for IR, BJ, and GM.